Highlights

A data-driven multiscale model for reactive wetting simulations

Jaideep Ray, Jeffrey S. Horner, Ian Winter, David J. Kemmenoe, Edward R. Arata, Michael Chandross, Scott A. Roberts, and Anne M. Grillet

- Developed a method to construct data-driven wetting model, from a small set of molecular dynamics simulations; studied wetting of molten silver-aluminum alloy on a Kovar™ substrate for brazing
- Performed molecular dynamics simulation to predict surface tension and wetting angle
- Calibrated probabilistic, data-driven surrogate model using limited training data and integrated wetting model into engineering-scale finite element brazing model
- Compared engineering model to experiment, identifying missing physics in simulations

A data-driven multiscale model for reactive wetting simulations

Jaideep Ray[a,*], Jeffrey S. Horner[b], Ian Winter[b], David J. Kemmenoe[b], Edward R. Arata[b], Michael Chandross[b], Scott A. Roberts[b], and Anne M. Grillet[b]

[a]*Sandia National Laboratories, PO Box 969, Livermore, CA, 94550,*
[b]*Sandia National Laboratories, PO Box 5800, Albuquerque, NM, 87185,*

Abstract

We describe a data-driven, multiscale technique to model reactive wetting of a silver-aluminum alloy on a Kovar™ (Fe-Ni-Co alloy) surface. We employ molecular dynamics simulations to elucidate the dependence of surface tension and wetting angle on the drop's composition and temperature. A design of computational experiments is used to efficiently generate training data of surface tension and wetting angle from a limited number of molecular dynamics simulations. The simulation results are used to parameterize models of the material's wetting properties and compute the uncertainty in the models due to limited data. The data-driven models are incorporated into an engineering-scale (continuum) model of a silver-aluminum sessile drop on a Kovar™ substrate. Model predictions of the wetting angle are compared with experiments of pure silver spreading on Kovar™ to quantify the model-form errors introduced by the limited training data versus the simplifications inherent in the molecular dynamics simulations. The paper presents innovations in the determination of "convergence" of noisy MD simulations before they are used to extract the wetting angle and surface tension, and the construction of their models which approximate physio-chemical processes that are left unresolved by the engineering-scale model. Together, these constitute a multiscale approach that integrates molecular-scale information into continuum scale models.

Keywords: reactive wetting, brazing, molecular dynamics, Markov process, continuum modeling, sessile drops

PACS: 47.11.Mn, 47.10.ab

*Corresponding author
Email address: jairay@sandia.gov (Jaideep Ray)

1. Introduction

Liquids wetting (or not wetting) solids are ubiquitous in nature, with examples including ethanol on glass or water on super-hydrophobic lotus leaves, respectively. Many industrial applications, such as manufacture of photographic films and soldering/brazing, rely on reactive wetting where the contact angle is mediated by reactions at the interface of the liquid and solid [1]. In these cases, the wetting dynamics are affected by multiple interacting physical processes including reaction kinetics, diffusion of reactants or reaction products, flow of the liquid and thermal transport. Since it is an inherently multi-physics problem, reactive wetting is still not well understood and manufacturing processes that rely on reactive wetting are difficult to model [1, 2]. An exemplar that embodies the complexities of reactive wetting is brazing, where two surfaces are joined by a filler metal that is heated above its melting point (and notably below the melting point of the substrates to be joined), and bonds them together (both physically and chemically) on cooling. Understanding and modeling these processes is quite challenging [3] due to the multiple physical and chemical processes that must be considered. Wetting by the filler metal depends not only on the temperature but also the composition of both the filler metal and the substrates. The compositions change over time, as components are liberated from the substrates through dissolution or, in the case of active brazing, chemical reactions, and absorbed by the filler metal. While studies of single metal fillers are abundant in the brazing literature [4], data are scarce for high fidelity studies of wetting of multicomponent alloys as a function of temperature and composition. This makes brazing an ideal application for the development of reduced order, data-driven models that can accurately predict the material properties that control reactive wetting behavior.

The motivation for our research is to lay a foundation for engineering-scale (millimeter to centimeter) simulations of a brazing process, with the specific goal of studying issues such as run-out where the filler material spreads beyond the surfaces being joined. Specifically, we seek a method to construct wetting models, trained on data from high-fidelity (HF) simulations, that can be integrated into engineering simulators of manufacturing processes. The exemplar system of interest consists of a Ag-Al braze filler joining Kovar™ (a speciality alloy composed of 29% Ni, 17% Co, 0.2% Si, 0.3% Mn, 0.01% C by mass, with the balance being Fe [5, 6]) surfaces, a system that has been previously investigated [7]. The primary technical challenge lies in modeling the reactive wetting at the filler-substrate interface in

a computationally efficient manner so that it may be reproduced within an engineering-scale simulation that cannot resolve all the relevant physics. Explicit resolution of such processes, using phase-field or molecular dynamics models, can only be performed for nanometer-sized drops [8, 9] (or smaller), and the simulations are very computationally expensive. Additional challenges lie in enforcing flow boundary conditions on the filler-substrate interface as it evolves.

In this paper, we describe a data-driven augmentation of conventional finite element models (FEM) that can be used to simulate active brazing at engineering scale. We begin with the assumption that macroscale reactive wetting at the filler-substrate interface depends on two fundamental interrelated phenomena, namely the surface tension of the liquid filler alloy $\sigma(T, Y)$ and its wetting angle on the substrate $\theta(T, Y)$, where T is the absolute temperature of the molten filler and Y is the composition of the filler alloy. Our hypothesis is that data-driven models of $\theta = F(T, Y; \mathbf{w})$ and $\sigma = G(T, Y; \mathbf{v})$ can be constructed based on HF simulations of a filler metal drop on a flat substrate surface. Here $F(T, Y, \mathbf{w})$ and $G(Y, Y; \mathbf{v})$ are the regression models and $(\mathbf{w}, \mathbf{v})$ are the regression models' parameters (or, loosely speaking, the sensitivity of θ and σ to T and Y). These models can be constructed by fitting to training data (TD) $(X = (T, Y)_i, Z = (\sigma, \theta)_i, i = 1 \dots N)$ by executing the HF simulations at a sampled set of $X = (T, Y)_i$ inputs and extracting $Z = (\sigma, \theta)_i$ from the simulation outputs. The FEM, augmented with the models $F(T, Y; \mathbf{w})$ and $G(T, Y; \mathbf{v})$, will be demonstrated by simulating a millimeter-sized silver sessile drop relaxing to equilibrium on a Kovar™ surface. In doing so, we will also describe how the boundary conditions are imposed in FEM at an evolving filler-substrate boundary.

The choice of the HF simulations is a difficult one. Ideally, the TD for the wetting model should include reactive processes and the formation of intermetallic phases (IMP) that are known to exist in the exemplar system [7]. However, the phase-field [8, 9] and reactive molecular dynamics (MD) simulations [10, 11] that can simulate these processes are computationally expensive and will not allow the assembly of TD in a timely fashion. Consequently, we will employ MD simulations using the embedded atom method (EAM; [12]), without reaction between the braze alloy and substrate, and in the process incur a modeling error. They key quantities for inclusion in the FEM are the surface tension and the wetting angle, and it is only the wetting angle that may be significantly affected by our choice of HF dataset. However, the wetting angle has contributions from the surface energy at the

liquid-gas, solid-gas and the liquid-solid interfaces, all of which could, depending on the extant reactions, incur a model-form error due to the absence of IMP in the TD simulations. This paper, in essence, will investigate whether this data-driven methodology can lead to stable and accurate engineering simulation, when embedded in a partial differential equation (PDE) continuum model. It will also quantify the PDE's model-form error (due to the approximate wetting models) and provide a path forward for ameliorating them via multi-fidelity modeling (discussed in Sec. 5.4).

The technical challenges presented here are (1) sufficient sampling of the (T, Y) space, that will necessarily use a limited number of samples N due to the computational cost of MD simulations (2) devising a proper functional form for $F(T, Y; \mathbf{w})$ and $G(T, Y; \mathbf{v})$ conditional on limited TD, (3) deciding on when an MD simulation has converged sufficiently (given limited computational resources/time) so that (σ, θ) may be extracted and (4) ensuring that the FEM, with embedded $F(T, Y, \mathbf{w})$ and $G(Y, Y; \mathbf{v})$, is stable and can reproduce, at least qualitatively, the process of a sessile drop equilibrating to its equilibrium shape. The sources of prediction error (of the data-driven models) are the fidelity of the MD simulations and the limited nature of the TD (and the consequent simplicity of $F(T, Y; \mathbf{w})$ and $G(T, Y; \mathbf{v})$). Identifying the relative importance of these sources of errors is a goal of this paper.

We will address the issue of constructing $F(T, Y; \mathbf{w})$ and $G(T, Y; \mathbf{v})$ using limited TD in two ways. First, we will ensure, in a data-driven manner, that the complexity of $F(T, Y; \mathbf{w})$ and $G(T, Y; \mathbf{v})$ is consistent with the information in the TD. Second, we will estimate the model parameters $\mathbf{w}$ and $\mathbf{v}$ as a joint probability density function (JPDF) so that we capture the uncertainty due to limited TD. Finally, we will devise a way to detect the convergence of fluctuating (i.e., time-dependent) MD data for θ, and extract a wetting angle *with a measure of the "extraction uncertainty"* that is then incorporated into the uncertainty estimates of $F(T, Y; \mathbf{w})$ and $G(T, Y; \mathbf{v})$ (specifically, the JPDF of $\mathbf{w}$ and $\mathbf{v}$). The convergence detection technique is based on approximating the noisy MD trace for $\theta(t)$ (where t represents time in the MD simulations) as a Markov chain (MC). If the MD simulation is determined to have not yet converged, our convergence detection method estimates how much longer the simulation is required to run to reach equilibrium.

The paper is laid out as follows. In Sec. 2 we review previous work on reactive wetting and the various techniques we use. In Sec. 3, we formulate the modeling problem (data-driven and the FEM). In Sec. 4, we describe the generation of the MD training and

experimental data. In Sec. 5, we present results of modeling σ and θ and the performance of the FEM. This section will also contain a comparison of FEM predictions to experimental measurements of a nominally pure silver drop on a Kovar™ surface, with the aim of estimating the magnitude of the model-form error in $F(T, Y; \mathbf{w})$ and $G(T, Y; \mathbf{v})$. We draw our conclusions in Sec. 6.

2. Literature review and background

In this section we review literature on experiments and MD simulations of reactive wetting, with emphasis on the fundamental physical processes. We also discuss the existing literature on FEM approaches (at engineering scales) that we employ, and the modifications necessary to include data-driven models of σ and θ. Finally, we discuss TD generation and data-driven modeling. Note that finite element studies of brazed joints, especially their residual stresses (due to a mismatch of thermal expansion coefficients of the materials involved), have been an active field of research (see Ref. [13] for a review), but they generally rely on experiments and/or temperature-tabulated material properties for specific filler-substrate combinations [14, 15, 16] rather than on the development of a generalized model for interfacial properties as presented here.

2.1. Reactive wetting and its models

The wetting of a solid metallic substrate by a molten metal or alloy can be of two types – inert (or passive) and reactive. In reactive wetting, the two phases (solid and liquid) may simply dissolve into each other or form a new intermetallic phase (IMP) that exists at the interface of the solid and the liquid [17]. Our system, Ag-Al on Kovar™ , undergoes reactive wetting [10, 7], with dissolution of elements and formation of an IMP of the form $(FeNiCo)_xAl$, where $1 < x < 3$, deposited in a reaction zone of about 10 μm thickness [7]. These wetting experiments were performed using millimeter-sized drops on a Kovar™ substrate.

Reactive wetting has been extensively studied but is not well-understood; see reviews in Refs. [18, 19, 17]. During reactive wetting, the change in composition of the substrates can be reaction-limited or transport-limited (i.e., diffusion of the active element – Al in our case – to the liquid-solid interface where the reactions occur). During the spreading of the drop, the solid-vapor-liquid interface (called the contact or triple line in 3D and triple point in 2D

descriptions) may initially travel along the bare substrate, but ultimately travels on a layer of the reaction products (RP) until equilibrium is reached. While the initial evolution of the interface shape is dominated by viscosity and inertial effects, the equilibrium configuration is determined by the balance of capillary forces. Young's equation, which relates the wetting angle (also called contact angle) θ to the surface energy of the substrate, surface tension of the liquid and the solid-liquid interfacial energy, should ideally be cast in terms of the liquid-RP interface rather than the native substrate. Since this energy is usually not known, there have been proposals to modify Young's equation to include the change in the free energy of the system caused by the production of the RPs [20, 21]. Thus by ignoring the RP when generating our TD, we will incur an error in our data-driven wetting models, but the magnitude is likely to be specific to our exemplar system.

Wetting can be improved (indicated by a smaller θ [18]) by the addition of trace elements to the filler alloy or the use of higher brazing temperatures; higher temperatures reduce viscosity and surface tension, and increase diffusion-driven transport, and thus accelerate the path to equilibrium. Ref. [22] modeled this convergence to equilibrium using an exponential in time whereas Ref. [9] observed more complex processes overlaid on the exponential. This auto-correlated behavior in time will play a central role in how we select a θ from MD simulations (discussed in Sec. 3.1). In addition, as the drop reacts with the substrate, it loses height without an equivalent change in its basal area [17, 18] (i.e., it penetrates into the solid as the solid substrate dissolves into the liquid filler material), and for nanometer-sized drops, may disappear completely [8]. This same phenomenon also affects MD simulations that are limited in the number of atoms that can be simulated. Additionally, as drop geometries can be difficult to extract in reactive simulations (see review in Ref. [19]) we use a fixed (i.e. non-reactive) substrate (see discussion below). In doing so, we incur model-form errors in our data-driven model for θ (see Sec. 5.4). Allowing the substrate to be flexible e.g., reactive, enhances wetting and reduces the wetting angle [10].

Detailed simulations of the dissolution and reactive wetting of a nanometer-sized drop on a substrate are often performed using phase-field models [8, 9, 23]. These are multicomponent (drop/substrate/RP), multiphase (solid/liquid/gas/RP) partial differential equation (PDE) models that use the Navier-Stokes equations to capture fluid dynamics, and the Allen-Cahn equations to track the evolution of the phases. The PDEs are solved using finite elements [8] or finite-differences [9], and due to the fine resolutions (and the consequent

computational cost) needed to resolve the reaction zone, are currently only possible for nanometer-sized drops. These simulations reproduce the exponential convergence of θ to equilibrium and the disappearance of the drop into the substrate. These simulations show the filler material penetrating into the substrate, forming a curved interface on which the IMP is deposited as it is formed. The simulations thus verified experimental findings [24] that caution against the naïve use of Young's equation as there is no fixed, planar substrate to use when defining the wetting angle. Ref. [8] also found that reactions promote wetting and the solid-liquid-vapor triple point moves faster in reactive systems (over the IMP) than non-reactive ones. IMP formation is controlled by the kinetics as well as the transport of the filler material and IMP to and from the filler-substrate interface. Similar simulations for an Al droplet on a Au substrate (a solder; Ref. [9]) provided an example of the proper use of Young's equation in a reactive system by defining it with respect to the curved IMP surface rather than the original, flat one. The simulation resolved the fluid mechanics inside the droplet as well as the reactions at the filler-substrate interface that lead to the formation of IMP; these kinetics were developed in Ref. [23]. They show the change in wetting angle when the IMP is formed, and the difference is significant (at least for the Al-Au system). The timescale of variation is in nanoseconds, implying that it is the equilibrium conditions that are of relevance in engineering-scale simulations, (see Fig. 5). They also found that the equilibrium wetting angle, at least for nanometer-sized droplets, depends on the size of the droplet. In addition, Ref. [9] shows that the wetting angles computed with spherical drops in 3D are larger than their counterparts computed using 2D simulations. Since we will use quasi-2D simulations (see below) to generate our training data, we may incur another model-form error, (likely an under-prediction of the wetting angle), in our approach (see discussion in Sec. 5.4).

2.2. Molecular dynamics simulations

Previous molecular dynamics simulations of brazing have focused on determining the degree of wetting and spreading of a liquid braze alloy on a solid substrate [25, 26, 27, 10]. These simulations have considered both passive wetting [25, 10], where the substrate is held fixed, and reactive wetting where diffusion and reactions between the drop and substrate are allowed [26, 10]. To simplify the development of these data driven models, this work has initially focused on fixed substrates. To explicitly calculate the wetting angle of a drop on a substrate, various approaches can be used. The wetting angle of a drop can be estimated

using Young's equation if the interfacial free energies of the system are known or can be calculated. Specifically, this requires the surface free energy of the solid substrate, surface tension of the drop, and solid-liquid interfacial free energy between the drop and substrate [28, 29].

The wetting angle can be computed from atomistic simulations, for instance, by taking the angle between the solid/liquid interface and liquid/vacuum interface at the triple point [10, 29]. The location of the triple point and the surface and drop profiles all fluctuate during dynamic simulations and introduce errors in the direct calculation of the wetting angle. An alternative approach to measure the wetting angle of a drop consists of fitting the contour of a drop to a circular sector (2D) or spherical cap (3D). By knowing the distance between the solid/liquid interface and the origin of the circle (2D) or sphere (3D) the wetting angle can be found [30]. This fitting method is robust to local fluctuations, but incurs fitting errors as we approximate a discrete boundary formed by molecules with a smooth curve or surface.

2.3. Data-driven modeling

Many processes that are not explicitly resolved by continuum simulators are empirically modeled using data-driven models, fit to experimental [31] or other high-fidelity [32] data. The functional forms for the data-driven fits can be motivated by theory or by flexible data approximators such as neural networks [32] or random forests [33]. Polynomials have also been widely used for this purpose in surrogate modeling (Chapter 13, Ref. [34]), especially in cases where the TD might be limited, as they allow their simplification (commensurate with the limited TD) using shrinkage (or an L_1 penalty) [35, 36] or by backward-forward stepwise elimination [37, 38]. Both these methods remove terms in the polynomial that are not significantly correlated with $Z = \{\theta, \sigma\}$. However, in these polynomial models the unknown model coefficients $\mathbf{w}$ and $\mathbf{v}$ are linearly related to Z, and if Z has uncertainties that can be modeled as a Gaussian, there exists an analytical method for propagating them back to the (Gaussian) JPDF for $\mathbf{w}$ and $\mathbf{v}$ (see Ref. [39]), as we will do. The method requires us to quantify our prior belief regarding $(\mathbf{w}, \mathbf{v})$ as Gaussians also.

A challenging feature of our TD-generating model (MD) is that, even when converged, the output consists of a value for $\theta(t_l)$, $l = 1 \dots L$ that strongly fluctuates around a steady-state value. On convergence, it should be possible to subsample (or thin) $\theta(t_l)$, $l = 1 \dots L$ to resemble independent draws around a central value with no temporal trend. In contrast,

before convergence, $\theta(t_l)$ is auto-correlated (in fact, per the discussion above, it has an exponential temporal trend) and can be thought of as a p^{th}-order Markov process. The two can be distinguished by testing whether (windows of) $\theta(t_l)$ resemble a first-order Markov chain (henceforth, MC) more than independent draws around θ_m. Details are in Ref. [40] and are summarized in Sec. 3.1, where we adapt this method to determine the convergence of MD simulations. The method uses a specified quality (i.e., level of certainty) with which the wetting angle must be extracted from the simulation, to evaluate whether the time-series $\theta(t_l)$, $l = 1 \dots L$ is sufficiently long to allow such a computation. If the time-series is too short, the method predicts how much longer the simulation must be run. An alternative approach is to compute windowed averages of $\theta(t_l), l = 1 \dots L$ (over Δt to smooth over statistical fluctuations) and check for an approach to a limiting θ_m. The latter approach, however, requires one to empirically determine Δt, and if convergence has not been reached, does not provide an estimate of how much longer to run.

2.4. Continuum modeling

The Cauchy momentum and continuity equations form the basis for continuum modeling of the fluid flow in brazing applications [41]. In the molten alloy (or filler material), the dynamic flow behavior is dictated by the density and viscosity. In addition, the method used to apply the boundary conditions is critical to both the dynamic and equilibrium behavior. The wetting speed at the solid/liquid contact line is dictated by a slip factor that overrides the traditional no-slip condition. The gas/liquid interface (top surface in Fig. 6) is a free surface that is allowed to move. At this boundary, the equilibrium behavior of the alloy is governed by the surface tension and the applied contact angle at the solid/gas/liquid interface.

Modeling free surfaces has been a historically challenging problem in computational fluid dynamics due to the discontinuity across the interface and the dynamic nature of moving surfaces. However, several advanced methods such as the volume of fluid [42], phase field [43], level set [44], and Arbitrary Lagrangian Eulerian (ALE) [45] have been shown to be accurate and stable in free surface simulation applications ranging from porous flow to propagating fluid surfaces. The popular level set method works by solving an independent function ϕ that is advected through an Eulerian grid. The phase interface can be defined as $\phi = 0$, with the positive and negative regions corresponding to the different phases. One difficulty with this approach is capturing the sharp interface location, as the mesh cannot be

specified with the interface in mind *a priori*. To resolve this, the conformal decomposition finite element method (CDFEM; [46, 47, 48]), which dynamically adds nodes along the interface into the background mesh rather than requiring interpolation of quantities between nodes, has been used in this work. This allows for sharper interface modeling as well as discontinuous representation of variables across the interface.

For wetting applications, such as brazing simulations, the traditional no-slip boundary condition is no longer applicable as the fluid needs to spread or contract along the solid surface. For finite element simulations, this requires refined modeling of the interface contact line along the solid surface. Typically, the slip condition is incorporated into the Navier-Stokes equations using a slip length, an extrapolated distance normal to the wall where the traditional no-slip condition could be theoretically applied [49]. For finite element simulations, this length can be recast as a dimensionless coefficient that is inversely dependent on the mesh size [50, 47]. In addition to slip modeling, at the solid/liquid contact line the surface energies of the respective phases must be accounted for through a contact angle. This has been achieved previously by incorporating a force at this contact line into the Navier-Stokes equations to drive the contact line toward the material-dependent wetting angle [51, 52]. While these methods can be used efficiently to model wetting applications, it is important to note that they still rely on accurate knowledge of the material properties; here we propose to incorporate these properties using data-driven models.

3. Formulation

In this section we describe a conservative method to gauge the convergence of a MD simulation generating wetting angles $\theta(t_l)$ (or the surface tension $\sigma(t_l)$). By conservative, we mean that it establishes a sufficient, but not necessary condition, i.e., if our technique indicates that the simulation has converged, then, with high probability, it has indeed done so; however, if the method fails to detect convergence, that does not imply that the MD simulation has not converged. This conservative method is needed to automatically track the generation of TD, as manual checking is simply not feasible for the multitude of MD simulations that are required. We also describe the method used to construct data-driven models i.e., $\sigma = F(Y_{Al}, T; \mathbf{w})$ and $\theta = G(Y_{Al}, T; \mathbf{v})$. The training data (TD) ($\{Y_{Al}, T, \sigma, \theta\}_i, i = 1 \dots N$) are generated using converged θ, σ. $F(:;:)$ and $G(:;:)$ are integrated into FEM simulations of sessile drops to ensure numerical stability and for model verification purposes.

3.1. Diagnosing convergence of a fluctuating MD data series

Consider a series of wetting angles $\theta(t_l) = \{\theta_l\}$, $l = 1 \ldots L$ calculated from an MD simulation. The wetting angle θ_l is determined at time t_l by fitting the drop shape to a spherical cap as described section 4.1. The sequence may indicate a systematic evolution/trend of θ and thus a lack of convergence to a non-zero θ [22, 9]. The sequence might also show an oscillation as the MD simulation approaches equilibrium in $\theta(t_l)$ (e.g., Fig. 2b); estimating the final wetting angle as the empirical mean θ_m can be biased depending on the stopping point of the sequence, the number of periods included in the empirical mean and the size of the oscillations (which could depict physical effects like capillary waves or a lack of convergence). Ideally the samples used in the mean should resemble independent draws from a stationary distribution, which could be obtained by thinning (i.e., subsampling) the sequence by k i.e., only every k^{th} item of the sequence is retained for estimation purposes. Note that if θ_l oscillates periodically about a central value, the method would indicate (erroneously) a lack of convergence. Note, too, that if there are many periods included in the median (or mean) and/or the oscillations are small, the bias may be sufficiently small to be acceptable. This makes the ideal case, of computing θ_m from independent draws, a conservative method for diagnosing convergence i.e., it is a sufficient, but not necessary, condition for convergence.

We assume that the sequence $\{\theta_l\}$ is a Markov chain (MC), and we wish to estimate a central value e.g., its median θ'_m, from it. We also desire that θ'_m lies between $\pm r$ of the true median q with confidence s i.e. $P(q - r \leq \theta'_m \leq q + r) = s$. If L is too short to allow this estimation, we desire an estimate of a length L' that will allow the estimation. The derivation below is adapted from our previous work on a generative model for uncorrelated complex networks [40], and is based on determining convergence of an MC [53, 54].

We compute the empirical median θ'_m from $\{\theta_l\}$ and convert it to a binary sequence $\{v_l\}$, where $v_l = 1$ if $\theta \geq \theta_m$ and $v_l = 0$ otherwise. Let $\{v_l^k\}$ be the $k-$thinned version of $\{v_l\}$, and let N_{mn} be the number of (m, n) transitions observed in $\{v_l^k\}$, $m, n \in \{0, 1\}$. N_{mn} is used to populate a 2×2 contingency table with entries normalized by the sequence length i.e. $(L/k - 1)$. Let $\widehat{N_{mn}}$ and $\widehat{\pi_{mn}} = \widehat{N_{mn}}/(L/k - 1)$ be the expected values of the table entries depending on whether we assume the sequence $\{v_l^k\}$ contains independent draws, or are generated by a first-order Markov chain (and thus can display autocorrelation). The goodness-of-fit of the data to these models is given by the likelihood-ratio statistic (G^2; see

Chapter 4.2 in Ref. [55]) and the Bayesian Information Criterion

$$G^2 = -2\sum_{m=0}^{m=1}\sum_{n=0}^{n=1} N_{mn}\log\left(\frac{\widehat{N_{mn}}}{N_{mn}}\right) \quad \text{or} \quad BIC = G^2 + N_p\log\left(\frac{L}{k}-1\right), \tag{1}$$

where N_p is the number of parameters in the model used to fit the table data. Log-linear models are generally used to model table data and estimate the transition probabilities $\pi_{mn}^{(I)}$ and $\pi_{mn}^{(M)}$ (see Ref. [40] for derivation) where superscripts I, M indicate an independent and a Markov process respectively. Drastically abbreviating the derivation in Ref. [40], we get

$$\Delta BIC = BIC^{(I)} - BIC^{(M)} = -2\sum_{m=0}^{n=1}\sum_{n=0}^{n=1} N_{mn}\log\left(\frac{\widehat{N_{mn}^{(I)}}}{N_{mn}}\right) - \log\left(\frac{L}{k}-1\right). \tag{2}$$

Here $\widehat{N_{mn}^{(I)}}$ is the expected number of (m,n) transitions if the binary sequence $\{v_l^k\}$ resembled independent draws from a distribution. A negative ΔBIC implies that the independent draws model fits the data better.

The log-linear models require that the sequence, of length $(L/k-1)$, is sufficiently long to provide good estimates and here we provide an estimate of how long is considered sufficient. Let θ_m^L be the empirical mean computed from the full sequence and θ_m^k from a $k-$thinned chain. Multiple θ_m^k can be computed for various levels of thinning (i.e., various ks) and will constitute draws from a normal distribution with mean q and variance ν^2. To ensure that the $k-$thinned sequence is sufficiently long, i.e., the empirical mean θ_m^k lies near the true mean with sufficient confidence or $P(q-r \le \theta_m^k \le q+r) = s$, or

$$\left(\frac{r}{\Phi^{-1}\{0.5(1+s)\}}\right)^2 = \nu^2 \tag{3}$$

where Φ is the cumulative distribution function for a standard normal distribution and s, r have been defined above.

Consider an $L-$step $\{\theta_l\}$ sequence that has been thinned by a factor k' and has become a first-order MC. Let L' be its length. The contingency table entries provide the transition probabilities of the 2-state Markov sequence $\{v_l^k\}$. The transition probabilities α and β can be computed trivially and ν^2 can be written as

$$\nu^2 = \frac{\alpha\beta(2-\alpha-\beta)}{L'(\alpha+\beta)^3} \quad \text{or} \quad L' = \frac{\frac{\alpha\beta(2-\alpha-\beta)}{(\alpha+\beta)^3}}{\left(\frac{r}{\Phi^{-1}\{0.5(1+s)\}}\right)^2}, \tag{4}$$

using Eq. 3. Thus the $k-$thinned sequence $\{\theta_l^k\}$ must be at least L' long to provide an estimate of q with the specified tolerance r. An implementation of this method is in the R package `mcgibbist` [56].

3.2. Constructing data-driven models

In this section, we describe the method by which we construct polynomial models for θ and σ. In our case, the filler material is primarily silver (Ag) with some aluminum (Al) and the composition Y is defined in terms of mass fraction i.e. $Y = \{Y_{Ag} = 1 - Y_{Al}, Y_{Al}\}$. Thus the independent variables in the models for θ and σ are (T, Y_{Al}). The convergence diagnostic described in Sec. 3.1 results in a $k-$thinned sequence $\{\theta_l^k\}$, a subset of which is used to compute the empirical mean and standard deviations (θ_m, ς). The subset of the $k-$thinned sequence that we use is the usually the last half, as by doing so we ignore the initial transients in $\theta(t)$ and $\sigma(t)$. This is repeated for many $(T_i, Y_{Al,i}), i = \ldots N$ combinations (the features in our TD) to yield (θ_i, ς_i) responses (the labels in our TD). Consider the vector $\mathbf{T} = \{T_i\}$. We scale the variables $\overline{T} = (T_i - \mathbb{E}(\mathbf{T}))/\sqrt{\text{Var}(\mathbf{T})}$, where $\mathbb{E}()$ and Var() denote the empirical mean and variance of TD values. The other variables are similarly scaled to get $\overline{Y_{Al,i}}$ and $\overline{\theta}_i$. We define the polynomial model simply as

$$\overline{\theta}_i = w_0 + w_1\overline{T}_i + w_2\overline{Y_{Al,i}} + w_3\overline{Y_{Al,i}}^2 + w_4\overline{T}_i^2 + w_5\overline{Y_{Al,i}} \times \overline{T}_i + \epsilon_i, \tag{5}$$

where ϵ_i is the fitting error, modeled as a Gaussian random variable with a zero mean and an unknown variance. The quadratic form is motivated by previous work [57] (which modeled the effect of temperature and surface roughness) and the tendency of trace elements to reduce the wetting angle [18]. Eq. 5 is fitted to the data via least-squares minimization, and simplified, via backward-forward stepwise elimination, to remove terms in the equation which do not contribute to $\overline{\theta}_i$ predictions. This results in a model

$$\overline{\boldsymbol{\theta}}^{(pred)} = \mathbf{A}\mathbf{w}, \qquad \mathbf{w} = \{w_j\}, \tag{6}$$

where j spans the terms in Eq. 5 that were retained after simplification and the superscript $(pred)$ denotes a model prediction. The columns of $\mathbf{A}$ contain the linear and quadratic terms of $\overline{T}_i$ and $\overline{Y_{Al,i}}$.

The uncertainty in the wetting angle estimate (ς_i) implies that there is a corresponding uncertainty in the estimates of $\mathbf{w}$ in Eq. 6. Since the model is linear in w_j, the uncertainty can be computed analytically (see Chapter 2, Ref. [39]). We create a prior model $\mathbf{w} \sim \mathcal{N}(\mathbf{w}_a, \Gamma_a)$, where Γ_a is diagonal and non-informative (i.e., the diagonal entries are large). The posterior distribution for $\mathbf{w}$ is given by $\mathbf{w} \sim \mathcal{N}(\widehat{\mathbf{w}}, \widehat{\Gamma})$ where

$$\begin{aligned} \widehat{\mathbf{w}} &= \mathbf{w}_a + \Gamma_a\mathbf{A}^T(\mathbf{A}\Gamma_a\mathbf{A}^T + \Gamma_\theta)^{-1}(\overline{\boldsymbol{\theta}} - \mathbf{A}\mathbf{w}) \quad \text{and} \\ \widehat{\Gamma} &= \Gamma_a\mathbf{A}^T(\mathbf{A}\Gamma_a\mathbf{A}^T + \Gamma_\theta)^{-1}\mathbf{A}\Gamma_a. \end{aligned} \tag{7}$$

Here $\Gamma_\theta = \text{diag}(\varsigma_i/\sqrt{\text{Var}(\boldsymbol{\theta})})$, $\boldsymbol{\theta} = \{\theta_i\}$ is a diagonal matrix denoting the uncertainty in $\overline{\boldsymbol{\theta}} = \{\overline{\theta}_i\}$. An identical process is followed to develop a model for the surface tension $\boldsymbol{\sigma}^{(pred)} = \mathbf{B}\mathbf{v}$, where $\mathbf{v} \sim \mathcal{N}(\widehat{\mathbf{v}}, \widehat{\Sigma})$.

3.3. The finite element model for sessile drops

To model the alloy deformation at engineering length scales, we use finite element modeling (FEM) as implemented in Sandia's Sierra/Aria Galerkin FEM code [58]. The three-dimensional domain $(8\times8\times8)$ mm includes two blocks corresponding to a solid substrate on which the alloy is allowed to spread and a multiphase alloy/atmospheric block resting above it. Only the boundary of the solid block interacts with the simulation, and all equations are solved on the fluid blocks. The maximum time step is set to 0.02 ms.

The alloy/atmospheric interface is represented using the CDFEM method [46, 47, 48]. With CDFEM, the interface is originally represented on the non-decomposed alloy/atmospheric block mesh using a level set field, (ϕ). This block is then conformally decomposed into separate alloy and atmosphere regions along the $\phi = 0$ isosurface.

Within the braze alloy and the atmosphere above it, the Cauchy momentum and continuity equations:

$$\rho\frac{\partial\bar{v}}{\partial t} + \rho\bar{v}\cdot\nabla\bar{v} - \bar{g} - \nabla\cdot\bar{\bar{T}} = 0 \tag{8}$$

$$\nabla\cdot\bar{v} = 0, \tag{9}$$

respectively, are solved to evaluate the pressure P and velocity vector $\bar{v}$. Here, ρ represents the density of the specific material phase (10,490 kg/m^3 for the alloy and 1.225 kg/m^3 for the atmosphere), $\bar{v}$ is the gravity vector (pointed towards the substrate), and $\bar{\bar{T}}$ is the stress tensor, which is defined as:

$$\bar{\bar{T}} = -P\bar{\bar{I}} + \mu\left((\nabla\bar{v})^\top + \nabla\bar{v}\right), \tag{10}$$

where μ is the viscosity (2.91 cP for the alloy and 0.0181 cP for the atmosphere) and $\bar{\bar{I}}$ is the identity tensor. At all outermost surfaces of the domain, an open flow boundary condition is applied with $P = 0$ and $\bar{n}\cdot\nabla\bar{\bar{T}} = 0$.

At the interface, surface tension is incorporated through a flux boundary condition:

$$\bar{n}\cdot\left(\bar{\bar{T}}_l - \bar{\bar{T}}_g\right) = -\sigma\bar{n}\nabla\cdot\bar{n}, \tag{11}$$

where $\bar{n}$ is the unit normal vector pointing out of the alloy and the subscripts l and g correspond to the alloy and atmospheric phases, respectively. Here, we incorporate the

species and temperature dependent surface tension $\sigma = G(T, Y_{Al}; \mathbf{v})$, as established in the preceding sections. At the substrate interface, fluid motion is enabled through a slip boundary condition applied tangentially along the substrate:

$$\bar{t}_w \cdot \bar{\bar{T}} \cdot \bar{n}_w = -\frac{\mu\beta}{\Delta x} \bar{v} \cdot \bar{t}_w, \tag{12}$$

where $\bar{t}_w$ is the unit tangent vector at the substrate surface, $\bar{n}_w$ is the unit normal vector at the substrate surface, Δx is the mesh size (0.15 mm background with 0.01 mm surface edge tolerance), and β is a non-dimensional slip factor (set as 0.01 for the alloy and 1.0 for the atmosphere). The influence of the slip parameter is analyzed in Appendix A. To prevent the drop from sliding around the substrate (due to numerical errors or asymmetrical mesh elements), a no-slip condition is applied to a small region of the alloy/substrate interface at the very center of the domain. The species and temperature dependent contact angle $\theta = F(T, Y_{Al}; \mathbf{w})$ is applied to the contact line (the intersection of the alloy/atmosphere interface and the substrate surface) through a force $\bar{f}_\theta$ term:

$$\bar{f}_\theta = \sigma \left(\bar{t}_w \cos\theta + \bar{n}_w \sin\theta \right). \tag{13}$$

The mean values $(\widehat{\mathbf{w}}, \widehat{\mathbf{v}})$ (see Eq. 7) are used to compute the nominal values of (θ, σ) used in the FEM.

We initialize the level set field as a hemispherical surface of radius 1 mm above the substrate. The level set is the advected through the non-decomposed mesh according to:

$$\frac{\partial \phi}{\partial t} + \bar{v} \cdot \nabla \phi = 0, \tag{14}$$

where $\bar{v}$ is the fluid velocity from the momentum equation. CDFEM is then used to update the conformal decomposition at every time step.

Thermal transport is coupled to the momentum equations through a separate convection-diffusion equation for the temperature T, using Fourier's Law for the diffusive flux:

$$\rho c_p \frac{\partial T}{\partial t} + \rho c_p \bar{v} \cdot \nabla T = \nabla \cdot (\kappa \nabla T). \tag{15}$$

Here, c_p is the specific heat capacity (arbitrarily set at 100 J/kg-K), and κ is the thermal conductivity (arbitrarily set at 100 W/m-K). The above equation was solved in both the liquid and gas phases, and a source term is applied as a flux boundary condition (1.5 W/mm^2)on the interface of the liquid with the solid wall. No flux is assumed for all other surfaces. Similarly, another convection-diffusion equation was coupled to the system

to represent chemical species conservation for aluminum, where we assumed the chemical species obeys Fick's Law for diffusion:

$$\frac{\partial C_{\mathrm{Al}}}{\partial t} + \bar{v} \cdot \nabla C_{\mathrm{Al}} = \nabla \cdot (D_{\mathrm{Al}} \nabla C_{\mathrm{Al}}) \,. \tag{16}$$

Here, C_{Al} represents the concentration of aluminum in the liquid, and D_{Al} is the aluminum diffusivity (arbitrarily set at 50 mm^2/s). Aluminum transport was only solved in the liquid domain with a flux condition (arbitrarily set at 0.3 mol/mm^2-s) at the solid wall interface and a no flux condition applied to the gas/liquid surface. Since incorporation of thermal and species transport presented here is intended as an illustrative example, the physical properties and fluxes were defined as to allow temperatures and concentrations to change significantly in the relatively short simulation time.

4. Data generation

In this section, we describe the method by which TD of MD simulations were generated. We also describe the experimental method by which we acquired the measurements of θ to estimate the model-form error in our MD simulations and therefore $F(T, Y_{Al}; \mathbf{w})$.

4.1. Generating the training data

To generate training data of θ and σ, as a function of (T, Y_{Al}), we first generate samples in 1150 $K \leq T \leq$ 1350 K and $0 \leq Y_{Al} \leq 0.043$ mass fraction (corresponding to a maximum mole fraction of 0.15), based on the temperatures and compositions observed in experimental studies of brazed joints [59]. The sampling was performed using a space-filling Halton sequence. Some of the (T, Y_{Al}) combinations were such that the filler material was not a liquid, and consequently we discarded these samples. Since the sampling design was space-filling, the excision of a subset of samples did not materially degrade the sample set. Fig. 1a shows the (T, Y_{Al}) samples that were retained, along with the (experimental) liquidus line that denotes the boundary above which the filler material is liquid. These 45 samples were used in MD simulations to compute the corresponding θ.

MD simulations were run using the embedded atom method [12] potentials developed by Zhou et al. to approximate an Ag-Al braze alloy and Kovar substrate [60]. Quasi-2D cylindrical droplets were considered. Note that quasi-2D simulations will slightly over-predict the wetting angle and surface tension relative to 3D simulations; Ref. [9] shows a

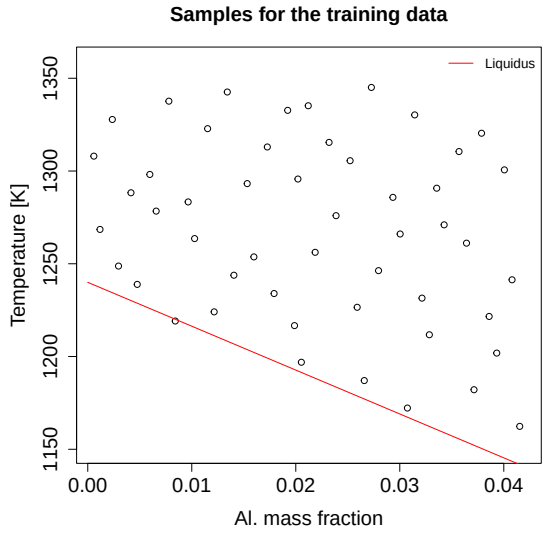

(a)

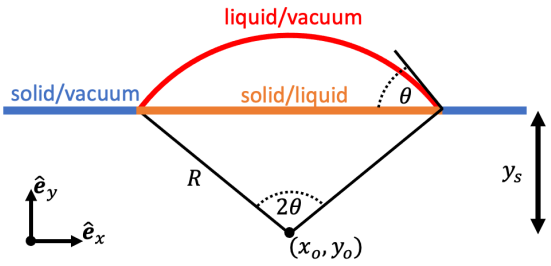

(b)

Figure 1: (a) Samples in the (T, Y_{Al})-space which were used to generate the TD for (θ, σ). The red line denotes an approximation of the experimental liquidus boundary; above it, the (T, Y_{Al}) combinations yield a liquid filler. (b) Relationship between the wetting angle of a droplet, θ, and the circle associated with the wetting angle defined by the radius of the circle, R, its origin, (x_0, y_0), and the distance of the origin of the circle to the surface y_s.

5% discrepancy in wetting angle between the two, computed using a phase-field model, for a Al droplet on a Au substrate. The droplets were placed on a (010) face-centered cubic substrate with dimensions of $78a_0 \times 13a_0 \times 8a_0$ corresponding to the droplet spreading direction, interface plane, and droplet width. The substrate was given a lattice parameter of $a_0 = 3.6$ Å. The initial wetting angle of the droplet was set to 90°. A Nose-Hoover thermostat (NVT) was used with a 100 fs temperature damping parameter. Each simulation ran for 50 ns with the timestep set to 2 fs and atomic positions were output every 20 ps. The wetting angle at a given time $\theta(t_l)$ was measured using the approach outlined by Nijmeijer et al. [30]. The functional form of the droplet's liquid/vacuum interface is that of a circular sector. As such, by fitting the liquid/vacuum interface to that of a circle, the wetting angle can be shown to be

$$\theta(t_l) = \arccos\left(\frac{y_s(t_l)}{R(t_l)}\right), \tag{17}$$

with y_s and R defined in Fig. 1b. To determine the contour of the liquid/vacuum surface, bins of width 3 Å were created along the $\hat{\boldsymbol{e}}_x$ direction. The position of the Ag atom with the highest y-component in a given bin was defined to be the height of the liquid/vacuum

interface for that bin. The solid/vacuum surface was defined as being 5 Å above the lowest value of all bins considered in the simulation to exclude surface states (i.e. the precursor foot that spreads before the main drop) along the solid/vacuum interface in the fitting of a circle to the surface.

The surface tension of the Ag-Al liquids was calculated from MD by creating a $10a_0 \times 10a_0 \times 20a_0$, $a_0 = 4.22$ Å, block of FCC atoms with periodic boundary conditions in the x- and y-directions and free surfaces for the z-direction. The block of atoms was made into a liquid by randomly displacing each atom -0.4 to 0.4 Å in each of the three Cartesian directions, and then running the simulation at 2500 K for 2 ps in an NVT ensemble with a Langevin thermostat. After the liquid was formed, the simulation was run for 4 ns at the desired temperature. The surface tension was calculated from the equation [61]

$$\sigma = \frac{V}{4A}\left(\langle\sigma_{xx}\rangle + \langle\sigma_{yy}\rangle - 2p\right), \tag{18}$$

where $\boldsymbol{V}$ is the volume of the system, $\langle\sigma_{xx}\rangle$ and $\langle\sigma_{yy}\rangle$ are the time-averages of the xx and yy components of the system's stress tensor, averaged over the final 2 ns of the simulation. A is the surface area between the liquid and vacuum. For mechanical equilibrium to be achieved for the planar interface between two fluids, the pressure in each fluid must equal p. In the case considered here, the interface between a vacuum and a liquid, We take $p = 0$. We note that within molecular dynamics simulations, averaged small, but finite, stresses normal to the vacuum/liquid interface can occur [62]. Substituting $p = \langle\sigma_{zz}\rangle$ into Eq. 18 changes the results of our surface tension calculations on average by 4 mJ/m^2. These finite values are within the average error of the calculation of $\langle\sigma_{xx}\rangle$ and $\langle\sigma_{yy}\rangle$ across all compositions and temperatures considered, 80 mJ/m^2.

4.2. Experimental methodology

Silver sessile drops on Kovar were formed by the following processes. Kovar sheet metal was sheared into 25 × 25 mm squares, degreased with acetone and isopropyl alcohol, and fired in a Thermal Technologies Inc. Astro AVF 430-SPL vacuum-hydrogen furnace for 2 hours at 1000^{o}C in a dry hydrogen atmosphere to reduce oxide on the surface. Brazing filler metal discs were cut from a pure silver rod. The discs weighed 0.42g ± 0.06. The discs were degreased in acetone and isopropyl alcohol. Sessile drops were formed by placing a silver disc on a Kovar square, placing a cylindrical Ti sheet metal "top-hat" on top of the sample to act as a getter and increase cleanliness, and brazed with the following parameters. The

furnace temperature was ramped up at a rate of 10^oC/min, with holds at 500^oC (30 min.), 900^oC (10 min.), and the brazing temperature (10 min.). Brazing temperatures of 1243, 1263, 1273, 1283, 1293, 1303 and 1323 K (970, 990, 1000, 1010, 1020, 1030, and 1050^oC) were investigated. The initial heating was conducted under high-vacuum, approximately 10^{-6} Torr, generated by a cryo-pump which allowed the molybdenum oxide on the heating elements to decompose and the O_2 be removed from the chamber. After 15 min. under high-vacuum at 500^oC, 9 Torr of gettered Ar (house liquid Ar source passed through a Ti gettering furnace, yielding Ar with approximately 0.3 PPB O_2) was added to the chamber to suppress Ag evaporation at brazing temperatures. With the Ar in place, temperature was ramped to 900^oC where a 10 min. hold increased temperature uniformity across the chamber, and then to the brazing temperature where it was held for 10 minutes. The furnace was then allowed to cool passively to room temperature.

The contact angle of the sessile drops was determined as follows. A "Depth-up" or "Z-stack" series of images focused at different heights was taken at 500× optical magnification on a Keyence VHX-6000 digital microscope and stitched into a 3D surface. Height profile data was then plotted along a line versus position and the flat plate and slope of the sessile drop were fitted with lines by eye using the Keyence software. The angle between these lines was taken as the contact angle. This process was repeated three times every 90^o around the circumference of the drop, for a total of 12 contact angle measurements. The average of these 12 measurements is the reported contact angle.

5. Results

In this section we develop models for θ and σ and embed them in an FEM to simulate the spreading of sessile drops.

5.1. Determining convergence and extracting θ and σ

In Fig. 2a, we plot the sequence $\{\theta_l\}$ from an MD simulation, of $L = 2501$ time-points where θ was computed (henceforth, called "ticks", and equal to a duration of 20 ps). The figure also shows a window-averaged version (with a window width of 200 ticks) that shows the convergence trend and the low-amplitude oscillations. We apply the convergence diagnostic of Sec. 3.1 with the quality requirement that the true median θ of the trace be computed, with 95% confidence, between the 40^{th} and 60^{th} percentile of the θ data. While

Run	L	L'	Correlation length	(θ, ς)
Well-behaved	2501	1709	17.6	$(22.81^\circ, 0.91^\circ)$
Ill-behaved	2502	4802	49.7	$(26.54^\circ, 1.70^\circ)$

Table 1: Statistics of the two runs shown in Fig. 2 (top). The "well-behaved" run attains its quality requirements within the number of timesteps simulated, primarily because of its smaller correlation length. The "ill-behaved" (unconverged) run does not, and results in a larger ς.

these lower and upper bounds may seem excessively generous, the actual variation of θ_l is small. The diagnostic yields that for the specified quality requirement, a subset of the run $L' = 1709$ is sufficient; further, it computes a correlation timescale of 17.6 ticks. Thinning the $\{\theta_l\}$ by 18 (the nearest integer greater than the correlation length), we get the samples that are plotted in red. We compute the mean and standard deviation of the last half of the red symbols to obtain (θ, ς) for this MD simulation. For the purposes of the data-driven model, θ can be thought of as an observation/measurement and ς, its measurement error. Per Sec. 3.2, only the last half of the samples, right of the vertical line in Fig. 2a, are used to compute (θ, ς). This information is summarized in Table 1. In Fig. 2b, we show an non-converged run (per the quality metrics specified to our conservative diagnostics). The time-averaged trace shows clear oscillations and the ideal run-length (L') indicates that the simulation ought to be run twice as long and thinned more aggressively to yield $\{\theta_l\}$ samples that are independent (see Table 1). Due to the computational cost, this was not done and the last half of the samples in Fig. 2b are used to compute (θ, ς). The mean and standard deviation computed for this run leads to ς that is almost twice as large as the previous one. These ς are explicitly captured in our data-driven model and its predictions. In Fig. 2c we plot the histogram of all θ in the TD; the median value is plotted with a solid vertical line and the first and third quartiles with dashed lines. We see that about 50% of the wetting angles lie between 21° and 27°. In Fig. 2d we see that the coefficient of variation ς/θ is small, with a median of about 0.045 i.e., despite the occasional inability of our MD simulations to meet the conservative quality requirements, the uncertainty in the simulated θ is rather small. The ill-behaved run is at the extreme right of the figure. Note that the net effect of "ill-behavior" is a larger uncertainty ς which is incorporated into the estimates of $\mathbf{w}$ via Γ.

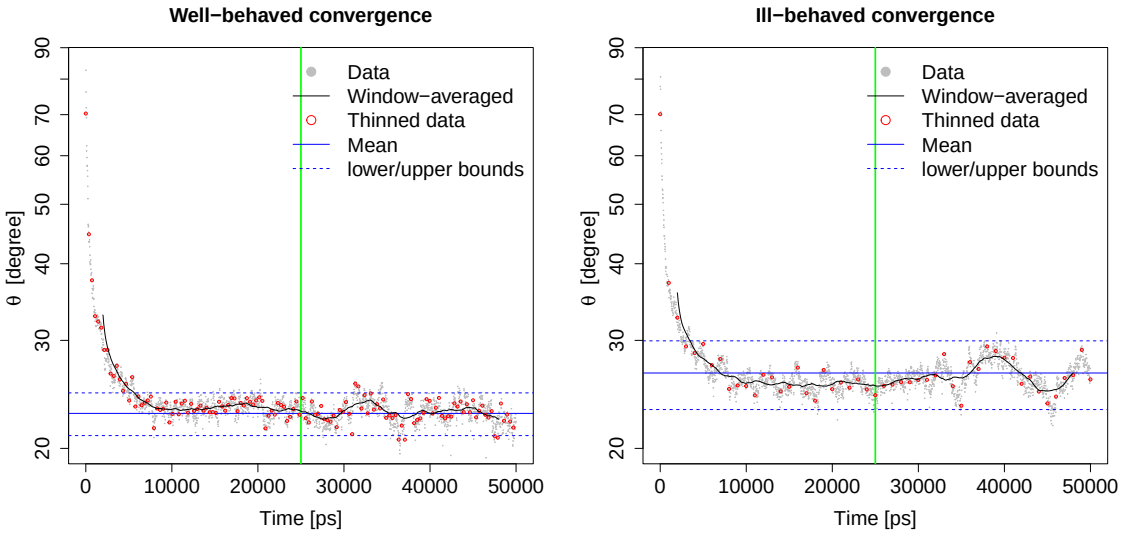

(a)

(b)

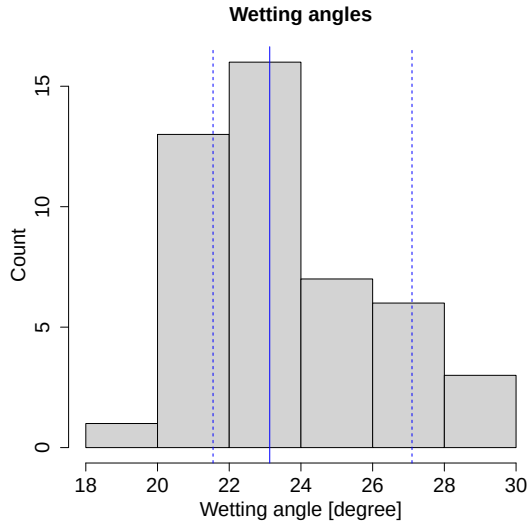

(c)

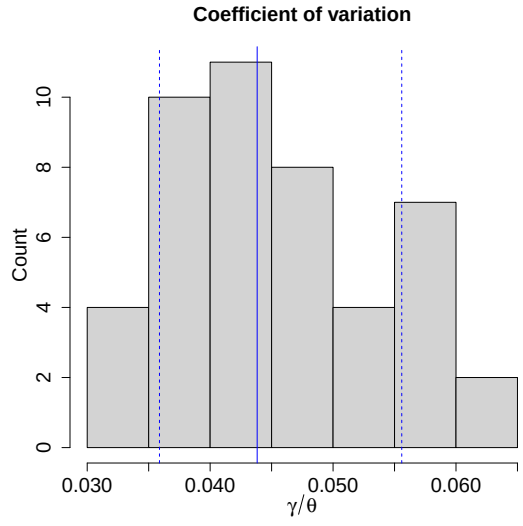

(d)

Figure 2: (a) A converged time series of θ for a run with ($T = 1250\ K, Y_{Al} = 0.042$). The dots are the θ computed at the timesteps that were saved (the "ticks"), the black solid line is the window-averaged version of the same and the red symbols are the θ that constitute independent draws. The final/converged values of the wetting angle and twice its uncertainty i.e., $(\theta, 2\varsigma)$ are also shown in blue. The last half of the samples, right of the vertical line, are used to compute (θ, ς).(b) The same, but for an "ill-behaved" (or unconverged) simulation time series (corresponding to a run with $T = 1337\ K, Y_{Al} = 0.0078$). The net effect of using this "ill-behaved" MD simulation is a larger ς when constructing data-driven models. (c) The distribution of the 45 θ in the TD. (d) The distribution of the coefficient of variation ς/θ. In both the figures, the median is plotted with a solid vertical line, and the first and third quartiles are plotted using dashed lines.

5.2. Data-driven models

The TD generated in Sec. 4.1 have features $(T_i, Y_{Al,i})$ and labels $(\theta_i, \varsigma_i), i = 1 \ldots N$. The first step in making a model for $\overline{\theta}$, per Eq. 6, is to determine the prior model i.e., the structure of $\mathbf{A}$. We propose a model of the form of Eq. 5 and fit it to the scaled TD i.e., to $(\overline{T}_i, \overline{Y_{Al,i}}, \overline{\theta}_i)$, while ignoring ς_i. The centering values $\mathbb{E}(:)$ for (T, Y_{Al}, θ) are $(1.268 \times 10^3, 2.222 \times 10^{-2}, 23.71^\circ)$ and the scaling ones $(\sqrt{\mathrm{Var}(:)})$ are $(47.35, 1.269 \times 10^{-2}, 2.280^\circ)$. The model is simplified via backward-forward stepwise elimination, which removes the w_4 term. Thus the scaled wetting angle $\overline{\theta}^{(pred)}$ is linear in (scaled) temperature, while being quadratic in $\overline{Y_{Al}}$. It yields $\mathbf{w}_a$, that is used in the prior distribution of $\mathbf{w}$ (see Eq. 7). The adjusted R^2 of the fit is 0.946 and a 20-way cross-validation resulted in a prediction error of 0.29°. Note that per Fig. 2c, the median θ is about 23° and the "measurement error" ς (Fig. 2d) is about 5%. Thus the prior model has an prediction error of about 1.2%, about a quarter of the measurement error. This is an estimate of one component of the model-form error in our data-driven model, and is due to the limited nature of the TD. The other component is due to the limitations of the MD simulations and will be quantified in Sec. 5.4.

Having determined the structure of $\mathbf{A}$ we proceed to compute the coefficients $\mathbf{w}$ via Eq. 7. The prior uncertainty on $\mathbf{w}$ is modeled as $\Gamma_a = \mathrm{diag}((3 * \mathbf{w}_a)^2)$ (i.e., we assume that the coefficient of variation is 3). Using Eq. 7, we compute

$$\begin{aligned} \widehat{\mathbf{w}} &= \{-0.57, -0.13, -0.75, 0.56, -0.17\} \\ \widehat{\Gamma} &= \begin{bmatrix} 10.1 & -1.2 & -0.6 & -5.8 & 5.4 \\ -1.2 & 6.0 & 1.3 & 0.8 & -2.0 \\ -0.6 & 1.3 & 6.1 & 0.4 & 0.9 \\ -5.8 & 0.8 & 0.4 & 7.0 & 1.5 \\ 0.54 & -2.0 & 0.9 & 1.5 & 7.9 \end{bmatrix} \times 10^{-3}, \end{aligned} \tag{19}$$

where $\widehat{\mathbf{w}}$ contains the intercept w_0 and coefficients of the $\overline{T}_i, \overline{Y_{Al,i}}, \overline{Y_{Al,i}}^2$ and $\overline{Y_{Al,i}} \times \overline{T}_i$ terms. $\widehat{\Gamma}$ contains the uncertainty in the $\mathbf{w}$ estimate. While it is diagonally dominant, it does display significant off-diagonal terms, denoting correlations between the various elements of $\mathbf{w}$.

In Fig. 3a we plot the $\widehat{\theta}^{(pred)}$. It is computed using $\widehat{\mathbf{w}}$ from Eq. 7, Eq. 6 and Eq. 19. All variables have been restored to their unscaled, physical values. The linear dependence on T and the quadratic dependence on Y_{Al} are clearly evident. Also evident is the muted

sensitivity of θ to T compared to Y_{Al} (see Eq. 5 and 19). We also plot the data points whose fitting errors are in the top 10^{th} percentile using symbols; two such points are below the shaded surface and not visible. These"badly modeled" points are the same ones that had the largest uncertainties in θ in the TD, as plotted in Fig. 2d. Note that the two axes are plotted in reverse order to illustrate the surface. The same figure is plotted as contours in the (T, Y_{Al})-plane in Fig. 3c; the liquidus is clearly visible and demarcates the (T, Y_{Al})-space where the filler material is a not a liquid. In Fig. 3b, we plot the uncertainty in $\theta^{(pred)}$ due to uncertain $\mathbf{w}$. We do so by taking 10,000 samples from $\mathbf{w} \sim \mathcal{N}(\widehat{\mathbf{w}}, \widehat{\Gamma})$ (and Eq. 19), generating realizations of $\theta^{(pred)}$ using Eq. 6, and computing the standard deviation as a function of (T, Y_{Al}). We see that the uncertainty in θ is largest at the boundaries; this is expected as the boundaries have data (to constrain the data-driven model) only on one side. In addition, the prediction uncertainty in the vicinity of the liquidus is also large. We also plot the ς of the same poorly fit points in Fig. 3a. Finally, in Fig. 3d, we plot a posterior predictive test. We use 1,000 samples of $\mathbf{w} \sim \mathcal{N}(\widehat{\mathbf{w}}, \widehat{\Gamma})$ and generate realizations $\theta^{(pred)}$ using Eq. 5 for $(T_i, Y_{Al,i}), i = 1 \dots 4$ examples that were held back from the TD. The box-and-whisker plots summarize the predictions. The values of θ from the TD are plotted as red symbols, with the 2ς bounds as whiskers. We see that in three out of four cases, the θ from the TD is contained within the first and third quartiles of the predictions, and the measurements, including the error bars, are contained within the whiskers of the predictions. However, the effect of the model-form errors (due to the limited TD) are also evident here - had these errors been negligible, the MD simulations' θ would have coincided with the median of the predictions.

An identical process was followed to construct the model $\sigma = G(T, Y_{Al}; \mathbf{v})$ for the surface tension. The behavior of σ in (T, Y_{Al})-space is simpler than θ and a less sophisticated sampling was used. The centering values $\mathbb{E}(:)$ for (T, Y_{Al}, σ) are $(1500, 4.5 \times 10^{-2}, 717.7)$ and the scaling ones $(\sqrt{\text{Var}(:)})$ are $(2.02 \times 10^2, 3.26 \times 10^{-2}, 31.35)$. The units of σ are mN/m. A prior model was fitted to the TD, which revealed that $v_3 = v_4 = 0$ i.e, the only relevant quadratic term in the model was $\overline{Y_{Al}} \times \overline{T}$. The adjusted R^2 of the fit is 0.98 and a 20-way cross-validation resulted in a prediction error of 4.75 mN/m. Note that the median σ in the training data was 717.7 mN/m, making the prediction error rather small. Having

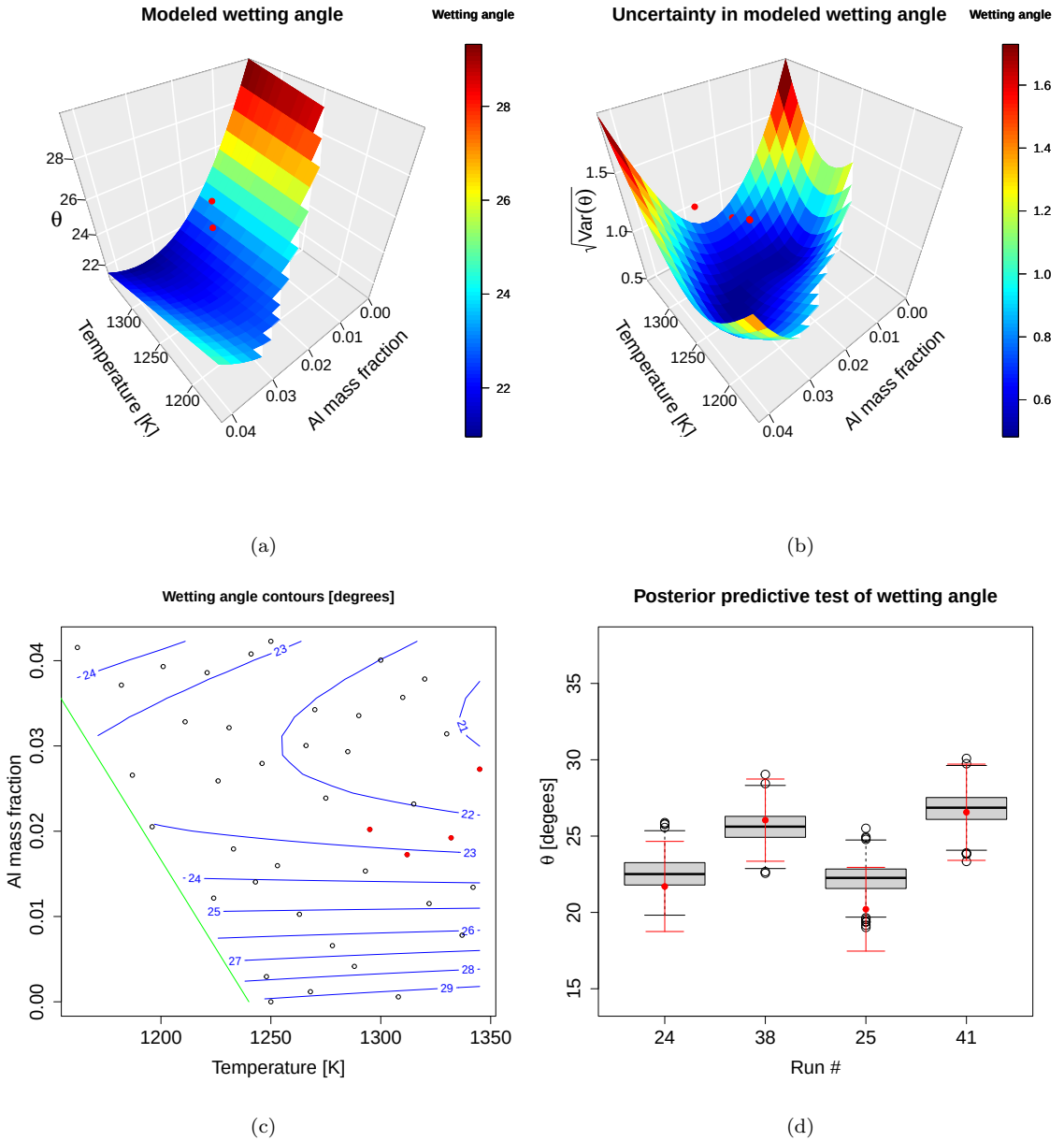

Figure 3: (a) Surface plot of $\widehat{\theta}^{(pred)}$. TD points that could not be modeled well are plotted in red. The unit of θ is degrees. (b) The uncertainty (standard deviation) in $\theta^{(pred)}$. (c) Contour plot of mean $\widehat{\theta}^{(pred)}$ in the (T, Y_{Al})-plane. (d) Posterior predictive test of four held-back θ, showing uncertainties in θ predictions versus the "measurement uncertainty". The red whiskers are 2ς bounds. The run numbers on the horizontal axis are insignificant and only denote the indices of the held-out data in the TD.

603 determined the structure of $\mathbf{B}$, we computed the probabilistic model per Eq. 7 to give

$$\begin{aligned} \widehat{\mathbf{v}} &= \{-0.0019, -0.8863, 0.4418, 0.0432\} \\ \widehat{\Sigma} &= \begin{bmatrix} 0.319 & -0.0140 & 0.0246 & -0.00135 \\ -0.0140 & 220.9 & -1.83 & 2.30 \\ 0.0246 & -1.83 & 228.0 & -1.07 \\ -0.00135 & 2.30 & -1.07 & 95.1 \end{bmatrix} \times 10^{-4} \end{aligned} \tag{20}$$

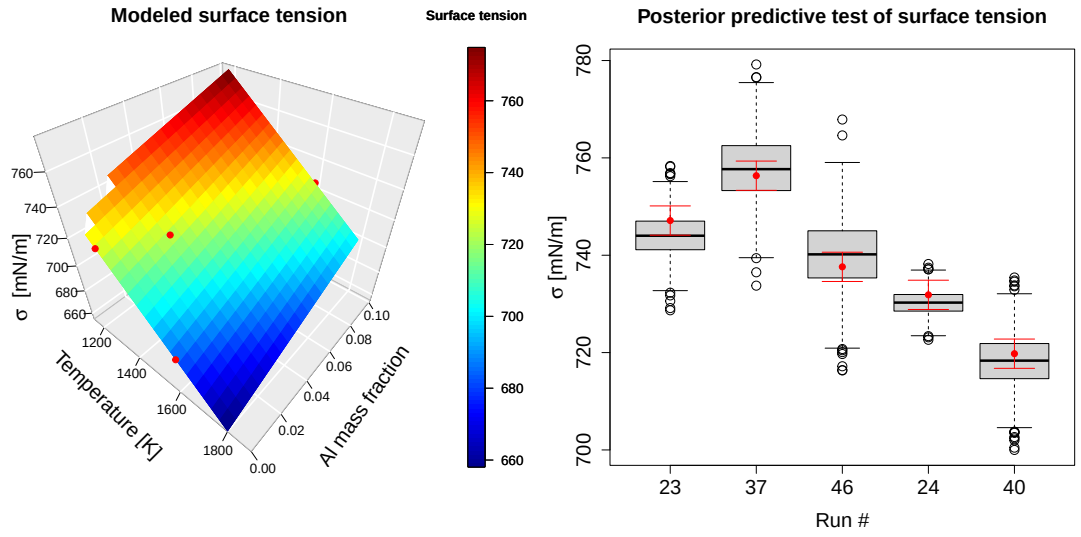

(a) (b)

Figure 4: (a) Surface plot of $\widehat{\sigma}^{(pred)}$ as a function of (T, Y_{Al}). The red dots are the worst modeled points. (b) Posterior predictive test of held-back σ, showing uncertainties in $\sigma^{(pred)}$ predictions versus the "measurement uncertainty" ς. The red whiskers are twice-standard-deviation bounds.

where $\widehat{\mathbf{v}}$ contains the intercept v_0 and coefficients of the $\overline{T}_i, \overline{Y_{Al,i}}$ and $\overline{Y_{Al,i}} \times \overline{T}_i$ terms. $\widehat{\Sigma}$ contains the uncertainty in the $\mathbf{v}$ estimate. $\mathbf{v}$ is seen, from $\widehat{\Sigma}$, to have insignificant correlations between themselves (off-diagonal terms are two orders of magnitude smaller than the diagonal ones). In Fig. 4a we plot the most probable prediction of $\sigma^{(pred)}$ i.e., $\widehat{\sigma}^{(pred)}$, which shows a strong linear trend. This is also evident from Eq. 20, where the coefficients for $\overline{T}$ and $\overline{Y_{Al}}$ are an order of magnitude larger than the quadratic term. The TD points with errors in the top 10 percentile are also plotted. In Fig. 4b we plot the posterior predictive results for 5 TD examples that were held-out when training the model. We see that the prediction uncertainties are larger than ς from the MD simulations, though all the data points (red symbols) are contained within the first and third quartiles of the predictions. In addition, the uncertainty in the predictions, as quantified by the inter-quartile range (the shaded box) as a proportion of the median prediction is quite small, around 1%. These plots show that the data-driven model for σ is more predictive than that of θ. Also note that these data-driven models are proxies for the MD simulation data; errors latent in the MD simulations themselves have yet to be quantified.

5.3. Sessile drop simulations with data-driven models

To demonstrate that these data-driven models can be successfully incorporated into finite element simulations, we simulated a hemispherical, Ag drop of radius 1 mm resting on a substrate. Initially, the drop is at 1150 K and contains no aluminum. Throughout the first half of the simulation, the drop is allowed to relax to an equilibrium state on the substrate that is dictated by the contact angle and surface tension. At 0.02 s, we apply a source term for the temperature and aluminum species at the substrate/drop interface, mimicking a chemical reaction. The aluminum and energy are allowed to spread within the drop via convection/diffusion. In typical brazing applications the heat transport occurs several orders of magnitude faster than the mass transport. However, for illustrative purposes we assigned fluxes that would allow the temperature and aluminum mass fraction along the contact line to vary on similar time scales. As this mimicked reaction progresses, the chemical composition and the temperature of the wetting surface change with time leading to an evolution of the contact angle as shown in Fig. 5. Note that the contact angle is post-processed based on the spatial mean of the unit normal vector along a reconstructed sliver of interface 0.001 mm above the substrate. We found the post-processed contact angle at this edge tolerance to be both not strongly influenced by the included area above the substrate and not strongly susceptible to numerical fluctuations associated with a smaller tolerance. The corresponding shapes of the drop at various times are shown in Fig. 6.

The FEM simulation demonstrates the ability to reproduce the wetting behavior of the alloy at a length scale commensurate with engineering applications. As shown in Fig. 5, the contact angle approaches the mean prediction from Eq. 6 and Eq. 19 that depends on temperature and aluminum mass fraction. The deviation between the two at the start of the simulation corresponds to the time needed for the drop to relax from its initial state, which is still occurring slightly at 0.02 s. The fluctuations in the FEM simulations can be attributed to discretization errors leading to localized errors in the post-processed contact angle and can be minimized by using a smaller time step as shown in Appendix B. As the aluminum mass fraction and temperature increase, additional deviation (about 0.6°) between the simulation and the mean prediction from Eq. 7 persists, indicating there is a slight lag for the simulations to respond to the new conditions. This deviation between the simulation and the analytical model can be minimized by using a finer mesh as shown in Appendix B.

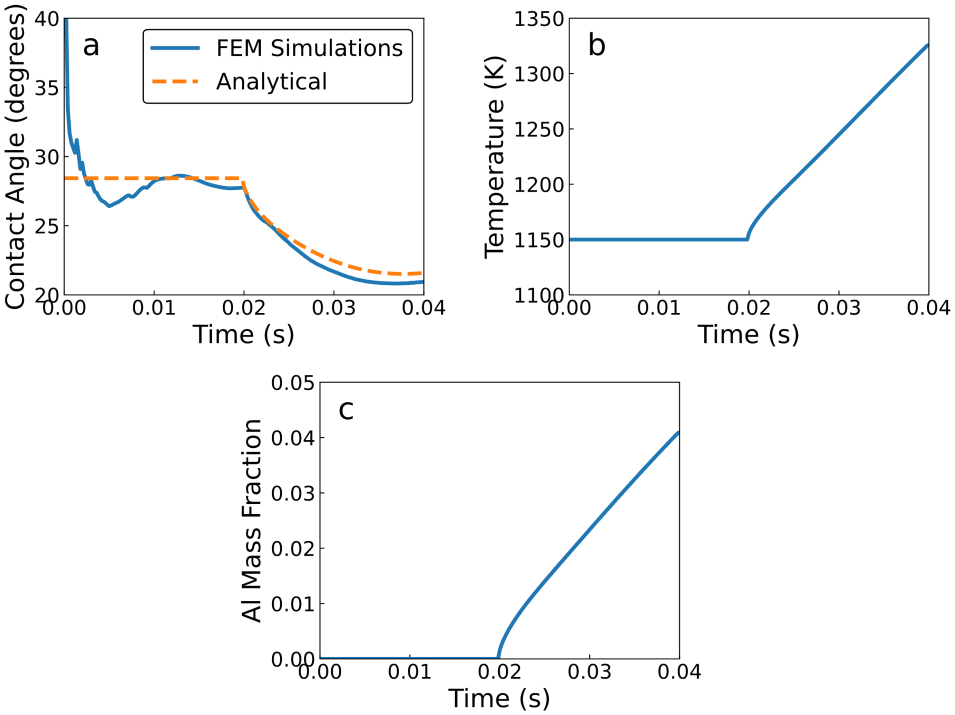

Figure 5: Results from FEM sessile drop simulations. (a) Post-processed contact angle as compared to the mean prediction (denoted analytical) from Eq. 6 and Eq. 19 for the prescribed temperature and aluminum mass fraction as plotted in (b) and (c), respectively. Note that the temperature and aluminum mass fraction are spatial means taken around alloy-atmosphere-substrate contact line.

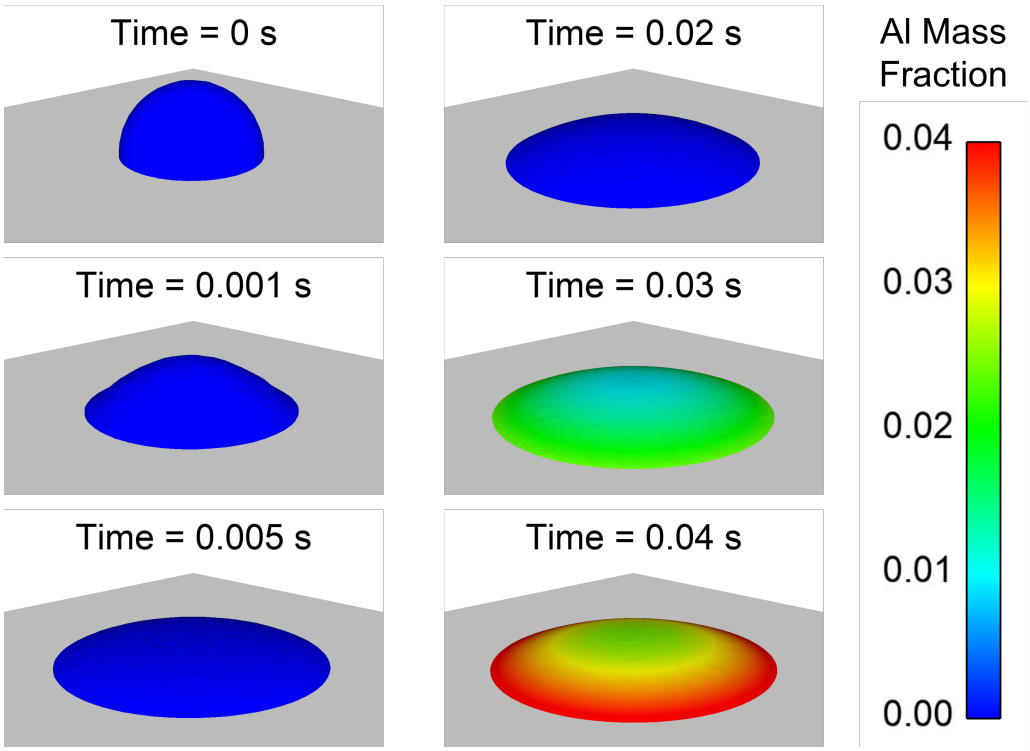

Figure 6: Depiction of FEM sessile drop shapes at different simulation times. The drop coloring corresponds to the aluminum mass fraction as indicated by the colorbar on the right.

5.4. Discussion

The discussion above focused on the development of the models $\theta = F(T, Y_{Al}; \mathbf{w})$ and $\sigma = G(T, Y_{Al}; \mathbf{v})$ and the shortcomings in their predictive skill versus the MD data. This first component of their model-form error is due to the simplicity of the data-driven model, which, in turn, is a consequence of the limited TD. However, these models have a second source for error from the MD simulations used to generate the TD.

The MD simulations generate θ using a quasi-2D model, rather than a 3D model. This was necessary for computational speed when assembling the TD and will result in smaller wetting angles compared to 3D simulations and experiments, as seen in Ref. [9], where the difference was about 5% for their Al-Au system. Further, the EAM potential is known to have difficulty predicting some multicomponent metallic alloy interactions [63, 64]. We consider this error acceptable to ensure the computational tractability of the TD; any errors in the resulting data-driven model can be corrected by assimilating experimental data via multi-fidelity modeling (see discussion below). In addition, our simulations assume a fixed substrate even though in reality the substrate dissolves into the molten filler, a phenomenon

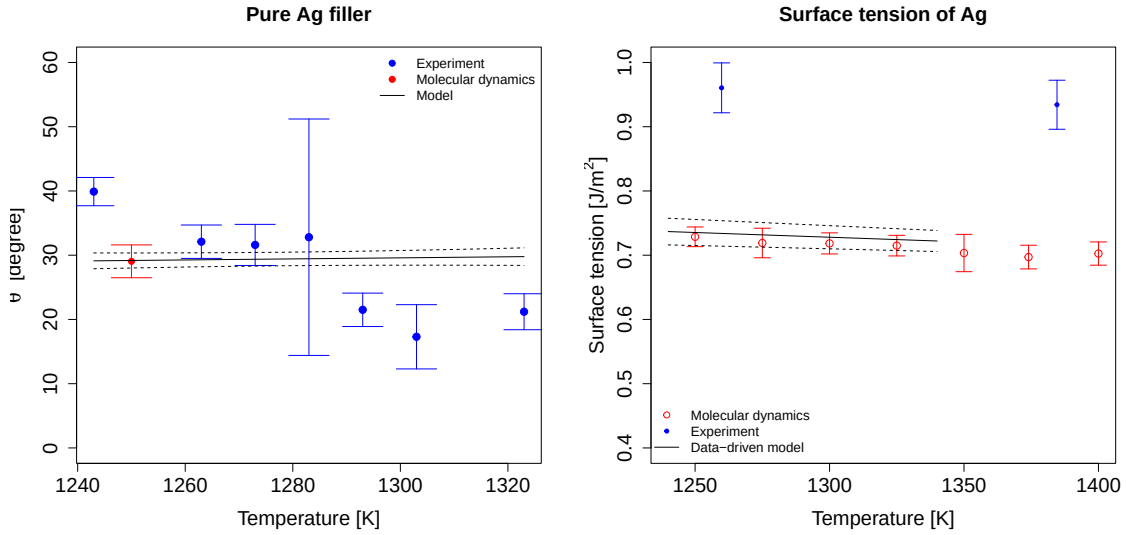

(a) (b)

Figure 7: (a) Comparison of experimental data for pure Ag on Kovar with model predictions. A molecular dynamics simulation of the wetting angle at 1250 K, taken from our training dataset, is also plotted. (b) Comparison of experimental data for pure Ag surface tension (from Ref. [65]), MD simulations and our data-driven model's predictions for σ. Error-bars are ± 2 standard deviation bounds. The solid line is the mean prediction using Eq. 7 and the dashed lines are the ± 2 standard deviation bounds computed using Eq. 7 and Eq. 19.

that our MD model does not currently capture. A fixed substrate keeps the braze/substrate interfacial free energy artificially high by preventing mixing of the substrate and braze. As a result, the fixed substrate condition overestimates the wetting angle[10]. The use of a fixed substrate implies that our θ could be larger than experiments. Finally, the experiments were conducted under 9 Torr pressure whereas the MD simulations were done in vacuum. We now investigate these errors by comparing against experimental data acquired with a pure Ag filler i.e., $Y_{Al} = 0$ wetting Kovar. Fig. 7a plots the experimental measurements of θ versus the model predictions (i.e., means, using Eq. 7 and Eq. 19). For the modeled results, the dashed lines show the ± 2 standard deviation bounds for the $\theta^{(pred)}$, computed using 100 samples drawn from Eq. 19 and Eq. 7. For the experiments, the average value of 12 measurements on each drop is plotted with symbols and the error-bars denote ± 2 standard deviation. The error bound for the MD data denotes the variation of θ over a time-window where it was computed. The experiment at 1280 K was repeated twice, and yielded somewhat different values of θ, leading to much larger uncertainty bounds.

Fig. 7a shows that the uncertainty in $\theta^{(pred)}$ is insignificant compared to the uncertainty of experimental measurements, as one would expect from Fig. 3b where the uncertainties are seen to be around 1°. Further, the model predicts hardly any change in the θ across the temperature range, also expected from Fig. 3a and the weak linear dependence of $\theta^{(pred)}$ on temperature. In contrast, the experimental data shows a clear temperature dependence. Note, also, that the data-driven model's prediction agree with the MD simulation results very well. In Fig. 7b we perform a similar comparison for σ compared to experimental measurements (obtained from Ref. [65]). Again, the MD and data-driven models agree in their predictions, but there is a distinct bias in the MD predictions when compared to measurements.

Model shortcomings and improvements: Fig. 7 exposes the shortcomings of adopting an approximate MD model that lacks reactive processes to generate the TD. It also raises the question of how to improve the $\theta = F(T, Y_{Al}; \mathbf{w})$ and $\sigma = G(T, Y_{Al}; \mathbf{v})$ models, under the condition that high-fidelity MD simulations (i.e., higher fidelity than the EAM model) are not possible e.g., due to resource constraints. The answer may lie in the structure of the discrepancy between the modeled and measured data seen in Fig. 7. Fig. 7a shows that the measurements vary around $\theta^{(pred)}$ as a smooth function of T. If the same structure holds true as Y_{Al} is varied, then it may be possible to add a correction $\delta\theta$ to $\theta^{(pred)}$, perhaps as a Gaussian Process. For σ, plotted in Fig. 7b, the discrepancy between the MD simulations and experimental data follows a simpler, almost linear trend in temperature, and an approach based on adding $\delta\sigma$ to $\sigma^{(pred)}$ may also also improve the predictive skill of the data-driven model. Improving the predictive skill of inaccurate, but computationally tractable, process-based models (our MD) by including a correction learned from sparse high-fidelity data is a type of multi-fidelity modeling used in many engineering problems [66]. Multi-fidelity wetting models, e.g., based on co-kriging, are feasible in principle but introduce new practical challenges. Primarily this requires the design and execution of a new, and far sparser, design of experiments, conducted via laboratory measurements or MD simulations that encompass reactions and can simulate the creation of IMP; these are under way. Secondly, data-driven multi-fidelity models are often Gaussian Processes or neural networks, which are far more difficult (from a solver and numerical stability viewpoint) and computationally expensive to integrate into a partial differential equation simulator vis-à-vis our polynomial fits; this is left to future work.

6. Conclusions

In this paper, we have developed a general technique for modeling the surface tension (σ) and wetting angle (θ) of a braze filler alloy on a substrate. These quantities are motivated by a desire for engineering-scale simulations of brazed joints, and in particular to investigate run-out i.e., the spread of the filler material beyond the surfaces being joined. In our case, the filler material is a silver-aluminum (Ag, Al) alloy and the substrate is Kovar™ . The dependence of σ and θ on the filler temperature (T) and composition (Y_{Al}) is captured by the model. We first summarize our findings and then discuss their ramification on being able to model brazing processes.

Summary of findings: The modeling process fundamentally consists of generating a training dataset of σ and θ for 50 (T, Y_{Al}) combinations by performing molecular dynamics simulations with EAM potentials, and capturing their dependencies via polynomial (nominally quadratic) fits $\theta = F(T, Y_{Al}; \mathbf{w})$ and $\sigma = G(T, Y_{Al}; \mathbf{v})$. The molecular dynamics simulations here do not capture all the physics occurring at the filler-substrate interface. We chose to begin with this simplified model due to its tractable computational cost, a necessity when a large (T, Y_{Al})-space has to be covered to generate a training dataset. In particular, we plan to extend this work to use chemically accurate (and far more computationally expensive) simulations, and therefore made the decision to limit computational cost as much as possible even with these simpler simulation techniques. We show how the (T, Y_{Al}) combinations may be generated in a space-filling manner, while removing some combinations may represent filler material that was not a liquid. We also discuss the simplification of the quadratic fits, commensurate with the information content of the limited training datasets. The simplified structure of the polynomials incur a model-form error, and consequently an uncertainty in the estimates of model parameters $(\mathbf{w}, \mathbf{v})$ when fitted to data. These parameter estimates are computed in a Bayesian manner i.e., as a joint probability density function. The uncertainty in the model predictions, and their disagreement with MD simulations are quantified. The models for θ and σ were integrated with an engineering-scale FEM, and used to simulate a drop initialized on a Kovar surface. The FEM reproduces the dynamics of the sessile drop reaching its equilibrium configuration in a qualitatively correct manner indicating that the integration of $F(T, Y_{Al}; \mathbf{w})$ and $G(T, Y_{Al}; \mathbf{v})$ did not destabilize the FEM or add noticeable stiffness to time-evolving simulations as they approach equilibrium. This was fortunate as these data-driven models interact with the slip

model on the solid surface as well as the force that drives the contact line to the equilibrium $\theta = F(T.Y_{Al}; \mathbf{w})$ angle.

Finally, we investigated the predictive skill of the data-driven model by comparing with experiments. The discrepancies seem to be almost entirely due to the missing physics in the simplified molecular dynamics simulations that are quasi-2D and use a fixed (i.e., non-reactive) substrate. We find that these discrepancies are far larger than the errors introduced by the simplicity of $F(T, Y_{Al}; \mathbf{w})$ and $G(T, Y_{Al}; \mathbf{v})$ arising from the limited nature of the training dataset. However, we find that the mismatch between experiment and model predictions shows autocorrelation (when $Y_{Al} = 0$) i.e., a smooth variation as a function of temperature T. If the same characteristic holds true for $Y_{Al} > 0$, the current models for σ and θ could be augmented in a multi-fidelity manner with a small number of experiments conducted at carefully chosen (T, Y_{Al}) combinations.

Ramifications on modeling brazing processes: The method described above is, in essence, a data-driven means of distilling results from MD simulations into a form that can be used in multicomponent, multiphase PDE models that can be used in engineering-scale simulations of reactive wetting e.g., brazing. As shown in Fig. 7, the model may need to be improved, perhaps by assimilating experimental data in a multi-fidelity manner to be predictive, but its inclusion into FEM appears to be straightforward and robust. The method can be extended to other configurations e.g., metal-ceramic brazed joints, by generating a training dataset using appropriate MD simulations. The process is rigorous, as it allows us to quantify the errors that arise due to modeling decisions. It therefore constitutes a multiscale simulation framework for brazing processes as well as more generally to wetting processes.

Active brazing is sometimes used to join metallic surfaces with ceramic ones, many of which contain aluminum. In these cases, the filler does not contain Al; rather, it diffuses out of the ceramic surface following a reaction with the braze alloy. We attempted to model this effect in our FEM simulation of a sessile drop with a point source. However, unlike our example where we were free to introduce an arbitrary amount of Al, a true brazing simulation would have to not only introduce the correct amount, but also validate that its transport inside the filler material is realistic. In addition, temperature and any components/elements that diffuse/dissolve out of the metallic surface, and are transported to the ceramic one, will doubtless affect the amount of Al that is released into the filler. Thus

a general modeling framework for active brazing is not feasible. However, the framework described in this paper may be sufficient for modeling the brazing of two metallic surfaces. Augmented with experimental data, via multifidelity models for θ and σ, it holds the promise of being predictive.

Acknowledgments

This article has been authored by an employee of National Technology & Engineering Solutions of Sandia, LLC under Contract No. DE-NA0003525 with the U.S. Department of Energy (DOE). The employee owns all right, title and interest in and to the article and is solely responsible for its contents. The United States Government retains and the publisher, by accepting the article for publication, acknowledges that the United States Government retains a non-exclusive, paid-up, irrevocable, world-wide license to publish or reproduce the published form of this article or allow others to do so, for United States Government purposes. The DOE will provide public access to these results of federally sponsored research in accordance with the DOE Public Access Plan (https://www.energy.gov/downloads/doe-public-access-plan). This paper describes objective technical results and analysis. Any subjective views or opinions that might be expressed in the paper do not necessarily represent the views of the U.S. Department of Energy or the United States Government.

References

[1] Yichuan Zhang, Hanqi Zhang, Mingming Guo, Joël De Coninck, and David Seveno. Reactive spreading dynamics of molten polymer liquids. Macromolecules, 56(3):1111–1121, 2023.

[2] G. Kumar and K.N. Prabhu. Review of non-reactive and reactive wetting of liquids on surfaces. Advances in Colloid and Interface Science, 133(2):61–89, 2007.

[3] S. Liu, D. L. Olson, G. P. Martin, and G. R. Edwards. Modeling of brazing processes that use coatings and interlayers. Welding J., 70:207–215, 1991.

[4] T. Iida and R.I.L Guthrie. The Physical Properties of Liquid Metals. Clarendon Press, 1999.

[5] Wikipedia. Kovar page. `https://en.wikipedia.org/wiki/Kovar`; accessed June 2023.

[6] Walter H. Kohl. Materials and Techniques for Electron Tubes. Reinhold Publishing Corporation, New York, NY, 1960.

[7] P.T. Vianco, C.A. Walker, D. De Smet, A. Kilgo, B.M. McKenzie, and R.L. Grant. Interface reactions responsible for run-out in active brazing: Part 1. Welding J., 97:35–S, 2018.

[8] W. Villanueva, W.J. Boettinger, G.B. McFadden, and J.A. Warren. A diffuse-interface model of reactive wetting with intermetallic formation. Acta Materialia, 60(9):3799–3814, 2012.

[9] Fei Wang, Andreas Reiter, Michael Kellner, Jürgen Brillo, Michael Selzer, and Britta Nestler. Phase-field modeling of reactive wetting and growth of the intermetallic Al_2Au phase in the Al-Au system. Acta Materialia, 146:106–118, 2018.

[10] M. Chandross. Competitive wetting in active brazes. Welding J., 94(5):169–175, 2015.

[11] E.B. Webb III, J.J. Hoyt, G.S. Grest, and D.R. Heine. Atomistic simulations of reactive wetting in metallic systems. J. Mat. Sci, 40:2281, 2005.

[12] S. M. Foiles, M. I. Baskes, and M. S. Daw. Embedded-atom-method functions for the fcc metals Cu, Ag, Au, Ni, Pd, Pt, and their alloys. Phys. Rev. B, 33:7983–7991, June 1986.

[13] Jaroslav Mackerle. Finite element analysis and simulation of adhesive bonding, soldering and brazing — An addendum: A bibliography (1996–2002). Modelling and Simulation in Materials Science and Engineering, 10(6):637, September 2002.

[14] M.I. Barrena, J.M. Gomez de Salazar, and M. Gomez-Vacas. Numerical simulation and experimental analysis of vacuum brazing for steel/cermet. Ceramics International, 40(7, Part B):10557–10563, 2014.

[15] W.C. Jiang, J.M. Gong, S.D. Tu, and H. Chen. Three-dimensional numerical simulation of brazed residual stress and its high-temperature redistribution for stainless steel plate-fin structure. Materials Science and Engineering: A, 499(1):293–298, 2009. Fifth International Conference on Physical and Numerical Simulations of Material Processing (ICPNS 2007) held at Zhengzhou, China, October 23-27, 2007.

[16] F. Meng, A. Liu, H. Sun, and M. Guo. Finite element analysis of thermal effects on brazed cold diamond grit. Transactions of the Indian Institute of Metals, 68:829—838, 2015.

[17] Nicolas Eustathopoulos. Wetting by liquid metals—application in materials processing: The contribution of the Grenoble Group. Metals, 5(1):350–370, 2015.

[18] Girish Kumar and K. Narayan Prabhu. Review of non-reactive and reactive wetting of liquids on surfaces. Advances in Colloid and Interface Science, 133(2):61–89, 2007.

[19] Qiaoli Lin, Kaibin Xie, Ran Sui, Dekui Mu, Rui Cao, Jinghuan Chang, and Feng Qiu. Kinetic analysis of wetting and spreading at high temperatures: A review. Advances in Colloid and Interface Science, 305:102698, 2022.

[20] Ilhan A Aksay, Carl E Hoge, and Joseph A Pask. Wetting under chemical equilibrium and nonequilibrium conditions. The Journal of Physical Chemistry, 78(12):1178–1183, 1974.

[21] V. Laurent, D. Chatain, and N. Eustathopoulos. Wettability of SiO_2 and oxidized SiC by aluminium. Materials Science and Engineering: A, 135:89–94, 1991. European Materials Research Society 1990 Spring Meeting on Metal Matrix Composites.

[22] J. C. Ambrose, M. G. Nicholas, and A. M. Stoneham. Dynamics of braze spreading. Acta Metallurgica et Materialia, 40(10):2483–2488, 1992.

[23] Fei Wang and Britta Nestler. A phase-field study on the formation of the intermetallic al2au phase in the al–au system. Acta Materialia, 95:65–73, 2015.

[24] E. Saiz, R.M. Cannon, and A.P. Tomsia. Reactive spreading: adsorption, ridging and compound formation. Acta Materialia, 48(18):4449–4462, 2000.

[25] M. Benhassine, E. Saiz, A. P. Tomsia, and J. De Coninck. Nonreactive wetting kinetics of binary alloys: A molecular dynamics study. Acta Materialia, 59(3):1087–1094, February 2011.

[26] Edmund B Webb III and Gary S Grest. Molecular dynamics simulations of reactive wetting. Scripta Materialia, 47(6):393–398, September 2002.

[27] Edmund B. Webb, Gary S. Grest, David R. Heine, and J. J. Hoyt. Dissolutive wetting of Ag on Cu: A molecular dynamics simulation study. Acta Materialia, 53(11):3163–3177, June 2005.

[28] Hao Jiang, Florian Müller-Plathe, and Athanassios Z. Panagiotopoulos. Contact angles from Young's equation in molecular dynamics simulations. The Journal of Chemical Physics, 147(8):084708, August 2017.

[29] Graham Saville. Computer simulation of the liquid–solid–vapour contact angle. Journal of the Chemical Society, Faraday Transactions 2: Molecular and Chemical Physics, 73(7):1122–1132, January 1977.

[30] M.J.P. Nijmeijer, C. Bruin, A.F. Bakker, and J.M.J. Van Leeuwen. A visual measurement of contact angles in a molecular-dynamics simulation. Physica A: Statistical Mechanics and its Applications, 160(2):166–180, 1989.

[31] Ricardo Macias-Salinas, Fernando García-Sánchez, and Otilio Hernandez-Garduza. Viscosity model for pure liquids based on Eyring theory and cubic EOS. American Institute of Chemical Engineers. AIChE Journal, 49(3):799, 2003.

[32] Julia Ling, Andrew Kurzawski, and Jeremy Templeton. Reynolds averaged turbulence modelling using deep neural networks with embedded invariance. Journal of Fluid Mechanics, 80:155–166, 2016.

[33] Pedro M Milani, Julia Ling, Gonzalo Saez-Mischlich, Julien Bodart, and John K Eaton. A machine learning approach for determining the turbulent diffusivity in film cooling flows. Journal of Turbomachinery, 140(2):021006, 2018.

[34] Ralph Smith. Uncertainty quantification: Theory, implementation and application. SIAM Computational Science & Engieering, 2014.

[35] J. Ray, Z. Hou, M. Huang, K. Sargsyan, and L. Swiler. Bayesian calibration of the community land model using surrogates. SIAM/ASA Journal on Uncertainty Quantification, 3(1):199–233, 2015.

[36] Jaideep Ray, Sophia Lefantzi, Srinivasan Arunajatesan, and Lawrence Dechant. Learning an eddy viscosity model using shrinkage and bayesian calibration: A jet-in-crossflow

case study. ASCE-ASME Journal on Risk and Uncertainty in Engineering Systems, Part B: Mechanical Engineering, 4(1), 2018.

[37] John H McDonald. Handbook of Biological Statistics, volume 2. Sparky House Publishing, Baltimore, MD, 2009.

[38] Jaideep Ray, Lawrence Dechant, Sophia Lefantzi, Julia Ling, and Srinivasan Arunajatesan. Robust Bayesian calibration of a k-ε model for compressible jet-in-crossflow simulations. AIAA Journal, 56(12):4893–4909, 2018.

[39] Clive D. Rodgers. Inverse Methods for Atmospheric Soundings: Theory and Practice. World Scientific Publishing Co. Pte Ltd, Singapore, 2000.

[40] Jaideep Ray, Ali Pinar, and C Seshadhri. A stopping criterion for Markov chains when generating independent random graphs. Journal of Complex Networks, 3(2):204–220, 2015.

[41] R. Byron Bird, Warren E. Stewart, and Edwin N. Lightfoot. Transport phenomena, Revised 2nd edition. John Wiley & Sons, Inc., 2006.

[42] C.W Hirt and B.D Nichols. Volume of fluid (VOF) method for the dynamics of free boundaries. Journal of Computational Physics, 39(1):201–225, jan 1981.

[43] Gunduz Caginalp. An analysis of a phase field model of a free boundary. Archive for Rational Mechanics and Analysis, 92(3):205–245, sep 1986.

[44] Rekha R. Rao, Lisa A. Mondy, David R. Noble, Harry K. Moffat, Douglas B. Adolf, and P.K. Notz. A level set method to study foam processing: A validation study. International Journal for Numerical Methods in Fluids, 68(11):1362–1392, September 2011.

[45] Henning Braess and Peter Wriggers. Arbitrary lagrangian eulerian finite element analysis of free surface flow. Computer Methods in Applied Mechanics and Engineering, 190(1-2):95–109, October 2000.

[46] Richard M. J. Kramer and David R. Noble. A conformal decomposition finite element method for arbitrary discontinuities on moving interfaces. International Journal for Numerical Methods in Engineering, 100(2):87–110, June 2014.

[47] David R. Noble, Alec Kucala, and Mario J. Martinez. A conformal decomposition finite element method for dynamic wetting applications. In Volume 1B, Symposia: Fluid Measurement and Instrumentation; Fluid Dynamics of Wind Energy; Renewable and Sustainable Energy Conversion; Energy and Process Engineering; Microfluidics and Nanofluidics; Development and Applications in Computational Fluid Dynamics; DNS/LES and Hybrid RANS/LES Methods. American Society of Mechanical Engineers, July 2017.

[48] Scott A. Roberts, Hector Mendoza, Victor E. Brunini, and David R. Noble. A verified conformal decomposition finite element method for implicit, many-material geometries. Journal of Computational Physics, 375:352–367, December 2018.

[49] Pierre Joseph and Patrick Tabeling. Direct measurement of the apparent slip length. Physical Review E, 71(3):035303, March 2005.

[50] Sashikumaar Ganesan, Sangeetha Rajasekaran, and Lutz Tobiska. Numerical modeling of the non-isothermal liquid droplet impact on a hot solid substrate. International Journal of Heat and Mass Transfer, 78:670–687, November 2014.

[51] V. E. B. Dussan. The moving contact line: the slip boundary condition. Journal of Fluid Mechanics, 77(4):665–684, October 1976.

[52] R. G. Cox. The dynamics of the spreading of liquids on a solid surface. Part 1: Viscous flow. Journal of Fluid Mechanics, 168(-1):169, July 1986.

[53] A. Raftery and Steven M. Lewis. Implementing MCMC. In W. R. Gilks, S. Richardson, and D. J. Spiegelhalter, editors, Markov Chain Monte Carlo in Practice, pages 115–130. Chapman and Hall, 1996.

[54] A. E. Raftery and S. M. Lewis. How many iterations in the Gibbs sampler? In J. M. Bernardo, J. O. Berger, A. P. Dawid, and A. F. M. Smith, editors, Bayesian Statistics, volume 4, pages 765–766. Oxford University Press, 1992.

[55] Y. M. Bishop, S. E. Fienberg, and P. W. Holland. Discrete multivariate analysis: Theory and practice. Springer-Verlag, New York, NY, 2007.

[56] Gregory R. Warnes and Robert Burrows. mcgibbsit: Warnes and Raftery's MCGibbsit MCMC diagnostic, 2013. R package version 1.1.0.

[57] W. Tillmann, J. Pfeiffer, and L. Wojarski. The apparent contact angle and wetted area of active alloys on silicon carbide as a function of the temperature and the surface roughness: A multivariate approach. Metallurgical and Material Transactions A, 46:3592—-3600, 2015.

[58] Sierra/SolidMechanics 5.10 ITAR users' guide. Technical report, sep 2022.

[59] P.T. Vianco, C.A. Walker, D. De Smet, A. Kilgo, B.M. McKenzie, P.M. Kotula, and R.L. Grant. Understanding the run-out behavior of a Ag-Cu-Zr braze alloy when used to join alumina to an Fe-Ni-Co alloy. In R. Gourley and C. Walker, editors, Proc. 6th International Brazing and Soldering Conference, 2015.

[60] X. W. Zhou, R. A. Johnson, and H. N. G. Wadley. Misfit-energy-increasing dislocations in vapor-deposited cofe/nife multilayers. Phys. Rev. B, 69:144113, Apr 2004.

[61] John G. Kirkwood and Frank P. Buff. The Statistical Mechanical Theory of Surface Tension. The Journal of Chemical Physics, 17(3):338–343, 12 2004.

[62] Wenbin Yu and D. Stroud. Molecular-dynamics study of surface segregation in liquid semiconductor alloys. Phys. Rev. B, 56:12243–12249, Nov 1997.

[63] R. A. Johnson. Phase stability of fcc alloys with the embedded-atom method. Phys. Rev. B, 41:9717–9720, May 1990.

[64] X. W. Zhou, R. A. Johnson, and H. N. G. Wadley. Misfit-energy-increasing dislocations in vapor-deposited cofe/nife multilayers. Phys. Rev. B, 69:144113, Apr 2004.

[65] I. Egry, E. Ricci, R. Novakovic, and S. Ozawa. Surface tension of liquid metals and alloys — recent developments. Advances in Colloid and Interface Science, 159(2):198–212, 2010.

[66] M Giselle Fernández-Godino, Chanyoung Park, Nam-Ho Kim, and Raphael T Haftka. Review of multi-fidelity models. arXiv preprint arXiv:1609.07196, 2016.

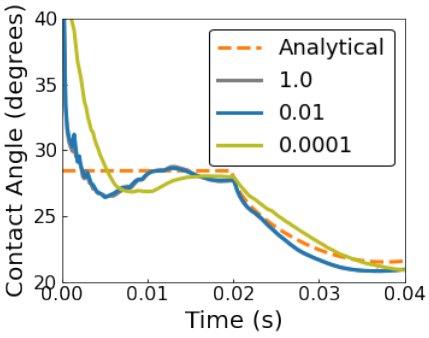

Figure A.8: Effects of varying the slip parameter β as compared to the analytical solution. The lines in the legend correspond to different values of β.

Appendix A. Slip parameter influence

To assess the influence of the semi-empirical slip parameter β on the FEM simulations, we conducted additional simulations with varying values of β. The results are shown in Fig. A.8 as compared to the analytical solution. Our results indicate that increasing β does not significantly affect the simulation as the dynamic behavior is restricted by the overall momentum balance. However, we found that decreasing β will result in delayed wetting behavior but may help to eliminate some numerical instabilities that arise during fast deformation of the interface.

Appendix B. Grid resolution study

The influence of mesh and time step sizing were assessed by independently varying the background mesh size from 0.25 mm to 0.15 mm and maximum time step from 0.1 ms to 0.02 ms, as shown in Fig. B.9. Increasing the mesh resolution leads to the simulation more closely aligning with the analytical solution. This is likely due to the fact as the background mesh sizing increases, the facets along the alloy-atmosphere-substrate contact line are more dependent on the capillary effects above the contact line, resulting in a lower post-processed contact angle. Despite the improved accuracy, simulations with increased mesh resolution are more susceptible to numerical instabilities and result in fluctuations of the contact angle. However, as the maximum time step decreases, these numerical fluctuations can be minimized.

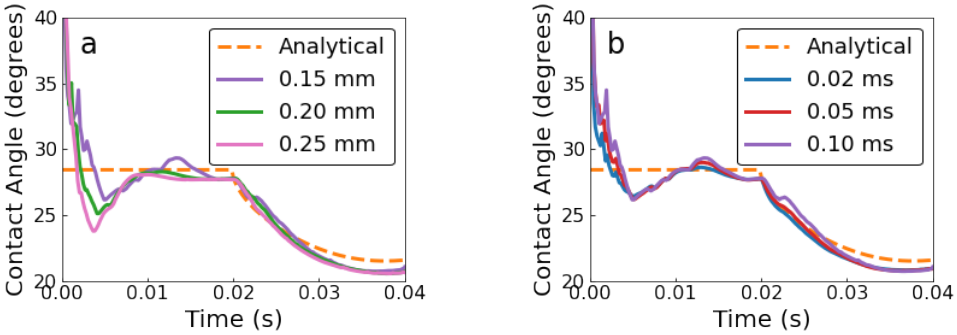

Figure B.9: Grid resolution study. (a) Effect of decreasing background mesh size for a fixed maximum time step of 0.1 ms. (b) Effect of decreasing maximum time step for a fixed background mesh size of 0.15 mm. The different lines in the legend correspond to mesh resolution (left figure) and time step size (right figure).